1	Laminated soil carbonate rinds as a paleoclimate archive of the Colorado Plateau
2	
3	Huth, T.E. ^{1*} , Cerling, T.E. ¹ , Marchetti, D.W. ² , Bowling, D.R. ³ , Ellwein, A.L. ⁴ , Passey, B.H. ⁵ ,
4	Fernandez, D.P. ¹ , Valley, J.W. ⁶ , Orland, I.J. ^{6,7}
5	¹ Department of Geology and Geophysics, University of Utah, Salt Lake City, UT 84112, USA
6	² Department of Natural and Environmental Science, Western Colorado University, Gunnison, CO 81231,
7	USA
8	³ School of Biological Sciences, University of Utah, Salt Lake City, UT 84112, USA
9	⁴ Rocky Mountain Biological Laboratory, Crested Butte, CO 81224, USA
10	⁵ Department of Earth and Environmental Sciences, University of Michigan, Ann Arbor, MI 48109, USA
11	⁶ Department of Geoscience, University of Wisconsin-Madison, Madison, WI 53706, USA
12	⁷ Wisconsin Geological and Natural History Survey, University of Wisconsin-Madison, Madison, WI
13	53705, USA
14	*Corresponding author: tehuth@umich.edu
15	Draft- April 28, 2020
16	Final Published Citation:
17 18 19 20 21	Huth TE, Cerling TE, Marchetti DW, Bowling DR, Ellwein AL, Passey BH, Fernandez DP, Valley JW, Orland IJ (2020) Laminated soil carbonate rinds as a paleoclimate archive of the Colorado Plateau. Geochim Cosmochim Acta. 282: 227-244. DOI: https://doi.org/10.1016/j.gca.2020.05.022
22	Highlights:
23	- A laminated soil carbonate rind from Utah acts as a paleoarchive from 35–5 ka
24	- We constrain soil conditions through time to enable quantitative interpretation
25	- Reconstructed vegetation correlates with regional pollen and soil records
26	- Reconstructed soil water $\delta^{18}O$ correlates with regional hydrologic records
27	- Laminated soil carbonates allow continuous, soils-based paleoclimate reconstruction

Abstract

Recent work suggests that the C- and O-isotope composition of laminated soil carbonate rinds can serve as a continuous paleoarchive of soil hydrology and vegetation over tens of thousands of years. However, while this archive can potentially provide quantitative reconstructions, most interpretations have thus far been qualitative. In this study, we show how modern soil data and "clumped" isotope paleothermometry can be leveraged to constrain the conditions of rind formation for a sample from the western Colorado Plateau, Utah, USA. We can thus quantitatively interpret rind isotope values as vegetation composition (%C₃-plants) and soil water oxygen isotope composition ($\delta^{18}O_{soil-water}$) over 35–5 ka. We validate the approach by demonstrating consistency between our record and other paleoarchives from the western USA. Laminated soil carbonate rinds therefore represent a new avenue for continuous, quantitative investigations of paleoclimatology, paleoecology, archeology, and modeling questions down to the scale of individual soils.

1 Introduction

Soil carbonate (CaCO₃) forms in drylands of the world and has been extensively used as a paleoarchive. This is because its stable isotope composition (C and O) can be tied to environmental conditions at the time of formation (Cerling, 1984). Soil carbonate carbon isotope composition (δ^{13} C) is primarily related to that of soil CO₂ via the photosynthetic pathway of organic material being respired and soil respiration rate during mineral formation (Cerling, 1984). For example, studies have interpreted δ^{13} C-soil carbonate data (hereafter, δ^{13} C_{sc}) in terms of landscape vegetation composition because plants using the C₃ and C₄ photosynthetic pathways are isotopically distinct. However, respiration rate is also an important consideration because soil CO₂ comes from two sources: biological respiration and the atmosphere. The abundance of soil CO₂ from each source can be described using a diffusion transport model (Cerling, 1984; Davidson, 1995). Thus, there exists a quantitative relationship between δ^{13} C_{sc} and plant composition.

The oxygen isotope composition of soil carbonate ($\delta^{18}O_{sc}$) is related to that of soil water ($\delta^{18}O_{soil-water}$) and the temperature of formation (Cerling, 1984). Soil water in turn is the result of meteoric precipitation and soil processes (e.g., evaporation, transpiration, mixing, etc.), both of which vary through time and influence $\delta^{18}O_{soil-water}$. As with the relationship between $\delta^{13}C_{sc}$ and $\delta^{13}C_{soil-CO_2}$, there exists a quantitative relationship between $\delta^{18}O_{sc}$ and $\delta^{18}O_{soil-water}$ (and ultimately $\delta^{18}O_{rain}$ and $\delta^{18}O_{snow}$). Interpreting $\delta^{18}O_{sc}$ in terms of $\delta^{18}O_{soil-water}$ is feasible as long as the temperature of mineral formation can be constrained (Kim & O'Neil, 1997). Estimating $\delta^{18}O_{rain}$ from $\delta^{18}O_{sc}$ is more complicated as modifying soil processes are more difficult to constrain (e.g., (Breecker, et al., 2009; Cerling, 1984; Oerter & Amundson, 2016; Quade, 2014; Quade, et al., 1989; Huth, et al., 2019)).

54

55

56

57

58

59

60

61

62

63

64

65

66

67

68

69

70

71

72

73

74

75

76

77

78

The relationships between soil carbonate isotope composition, vegetation type, and climate have been extensively used for paleoclimate and paleoecology research. In general, applications have focused on questions involving change on >0.1-1 Ma timescales. This is because most studies utilize soil carbonate in the form of nodules, which due to their complicated internal age structure are generally conducive to bulk estimates of environmental conditions for the life of the soil (e.g., 1-100s ka). As soil formation periods are generally of the same order of magnitude or greater than the duration of most late Quaternary climate fluctuations, there have been considerably fewer applications of soil archives to these shorter timescales as compared to speleothems and lake cores (e.g., (Quade, 2014; Birkeland, et al., 1991); but see also the stacked paleosols of the Chinese Loess Plateau; e.g., (Sun, et al., 2006)). The few soil studies available have used bulk isotopic measurements in (paleo-)soil sequences to infer 1–10 kyr environmental changes (Cole & Monger, 1994; Liu, et al., 1996). To acquire continuous, high-resolution (100s yr/measurement) records of late Quaternary climate and vegetation change, recent studies have focused on soil carbonate formed as laminated rinds on the bottoms of clasts (hereafter "rinds," but depending on soil context referred to as "pedothems;" (Oerter, et al., 2016)). Rinds are a desirable record type because they frequently preserve an intact, dateable stratigraphy, record 10–100s kyr of change, are common in arid and semi-arid regions worldwide, provide a definitively local signal, and allow for

identification of changes in vegetation and climate/soil conditions from a single, internally consistent record (Oerter, et al., 2016; Huth, et al., 2019; Cerling, 1984). Therefore, in addition to providing an independent view of climate and vegetation change, rinds can potentially provide 10s kyr of high-resolution (100s yr/measurement), continuous paleoclimate data over a range of elevations.

The basic effectiveness of laminated rinds as a proxy has been explored by researchers in Wyoming, Syria, Turkey, and Siberia as well as by our group working in Utah (Oerter, et al., 2016; Pustovoytov, et al., 2007; Pustovoytov, et al., 2007; Huth, et al., 2019). These researchers used a variety of methodologies to date (radiocarbon vs. U/Th dating) and sample [hand drilling, micromilling, Secondary Ion Mass Spectrometry (SIMS)] rinds of mm to >10 cm thickness. Study landforms varied considerably, encompassing river terraces, debris flows, alluvial fans, and archeological sites (stone construction and pottery sherds).

While previous studies have emphasized the potential for rinds to provide continuous paleoclimate and paleovegetation information, most interpretations have thus far been necessarily qualitative. This is because previous studies lacked direct information about the timing and conditions of soil carbonate formation today and in the past. As the timing of soil carbonate formation is seasonally biased (Huth, et al., 2019; Oerter & Amundson, 2016; Breecker, et al., 2009), without constraining the (1) temperature and (2) soil respiration (i.e., autotrophic plus heterotrophic respiration) during mineral formation, it was challenging for previous researchers to quantitatively interpret the records.

In this study, we build upon previous work using soil carbonate rinds by demonstrating a methodology to obtain quantitative estimates of past $\delta^{18}O_{\text{soil-water}}$ and vegetation composition (%C₃ plants) from a soil carbonate rind. We explored the proxy at one site on the Colorado Plateau and provide a detailed record of climate and vegetation change (100s yr resolution over 35–5 ka). First, we describe the study setting, our prior work constraining the modern timing of soil carbonate formation, the paleorecord sampling strategy, and the methodology for reconstructing paleoclimate and vegetation change. We then present the results, discuss the validity of our interpretations in the context of previous paleoclimate and vegetation inferences, and conclude with an outlook for the methodology.

2 Study setting and methodology

Because a primary motivation of this study is to describe a new methodology, we focus here on the portions of the study design, sample analyses, and methodology relevant to reconstructing $\delta^{18}O_{soil\text{-water}}$ and vegetation composition through time. Full details of the sample analyses can be found in the Supplementary Appendix.

2.1 Climate and geologic setting

The Fremont River Valley, which contains the town of Torrey, Utah, USA, has a semiarid climate, receiving ≈260 mm of annual precipitation (Prism Climate Group, 2018) (Fig. 1; SI Appendix, Fig. S1). Meteoric precipitation is seasonally biased (45 % in JASO) with summer rainfall derived from southerly winds usually associated with the North American Monsoon (NAM, (Higgins, et al., 1997)). NAM related rainfall may be orographically enhanced by the site's location between mountain ranges to the north and south. Winter precipitation is brought by cold frontal storms associated with westerly winds. Temperature seasonality is large at Torrey; average daily temperature (average low/high) in January and July are -3.7 °C (-11.3/3.9 °C) and 20.2 °C, (11.4/28.9 °C), respectively.

The study area features a number of soils developed on stable mid- to late Pleistocene geomorphic surfaces related to mass movement deposits (Fig. 2a, SI Appendix Fig. S1) (Marchetti & Cerling, 2005; Marchetti, et al., 2005). The surfaces are primarily composed of large (0.2 to > 1 m) trachyandesite boulders within a finer-grained matrix of mixed sedimentary units (mudstone, limestone, sands, silts, chert pebbles, etc.). This study takes place on the Teasdale Bench, which is 2100 m above sea level (masl; TB − N 38.302°, W 111.478°; SI Appendix, Fig. S1). Soils in this region have accumulated dust through time and have significant calcite accumulation consistent with local climate (≥Stage III carbonate morphology; SI Appendix, Fig. S1; (Huth, et al., 2019; Gile, et al., 1996; McFadden, 2013)). The laminated rinds of this study formed on the bottoms of large (1 m b-axis) boulders and had an identifiable stratigraphy useful for dating (Fig. 2a and 2b; (Huth, et al., 2019)). Because large boulders

often show surface coloration associated with *in situ* soil horizons (Fig. 2a), we could constrain the depth of formation for rinds examined in this study to >40 cm by only collecting rinds from the largest boulders (Huth, et al., 2019). Knowledge of the depth of rind formation is important, because soil carbonate formed at this depth is unlikely to have a significant influence from atmospheric CO_2 , meaning that the $\delta^{13}C_{sc}$ will primarily reflect changes due to vegetation type (Cerling, 1984). Additionally, targeting large boulders for sampling ensured that rinds formed in a stable position and were not exhumed during rind formation. As only about one in thirty pedogenic rinds appeared suitable for dating (i.e., had visually continuous stratigraphy) and rinds on the bottoms of \approx 1 m boulders can only be accessed *in situ* with a backhoe, we necessarily collected rinds from boulders that were excavated during highway construction on the Teasdale Bench. The selected rind, Pendant 11-8, was chosen because of its continuous stratigraphy and few large void spaces. All analyses were performed on different pieces of this rind (Fig. 2, SI Appendix, Fig. S2).

2.2 Modern soil environment and the timing of soil carbonate formation

Cycles of temperature and precipitation at Torrey cause changes in the soil environment and its associated C- and O-isotopes. In turn, the changes in soil environment control the timing of soil carbonate formation and its isotope ratios. Soil carbonate formation seasonality is therefore an important consideration in interpreting isotopic variability and we previously investigated the modern soil environment of this region as a prelude to this study (Huth, et al., 2019). As a guide to readers, we describe the soil environment at 40 cm depth as analogous to the depth of rind formation (Fig. 3).

The modern soil at Torrey exhibited annual changes in soil CO₂, temperature, and moisture (Fig. 3). Soil CO₂ followed a roughly sinusoidal pattern and was lowest in winter (1,000 ppm) and highest in summer (3,000 to 8,000 ppm). Soil temperature also exhibited a roughly sinusoidal pattern and was lowest in winter (0 °C) and highest in summer (25 °C). The timing of soil moisture changes was consistent with infiltration during snowmelt events (late winter-early spring) and during large rain events during the mid- to late summer (Huth, et al., 2019).

In conjunction with these soil environment changes, the values of $\delta^{13}C_{\text{soil-respiration}}$, $\delta^{18}O_{\text{rain}}$, $\delta^{18}O_{\text{snow}}$, and $\delta^{18}O_{\text{soil-water}}$ also varied (Fig. 3a and 3b). The $\delta^{13}C$ of soil respired CO₂ varied in phase with soil CO₂ concentration, exhibiting C₃-like values in the winter (-25 % VPDB) and values consistent with mixed C₃–C₄ respiration in the summer (-21 to -16 % VPDB). Average monthly values of $\delta^{18}O_{\text{rain}}$ and $\delta^{18}O_{\text{snow}}$ varied from -18 % VSMOW in the winter to -5 % VSMOW in the summer. However, $\delta^{18}O_{\text{soil-water}}$ showed more muted changes, ranging from \leq -11 % VSMOW in the winter to >-6 % VSMOW in the summer (note few data points are available). Isotopic evidence of evaporation was found at all investigated soil depths, but was most prominent in summer (Huth, et al., 2019).

To complement these modern observations, we also used "clumped" isotope analyses (Δ_{47}) to estimate the Holocene temperature of soil carbonate formation [T(Δ_{47})] (Eiler, 2007; Ghosh, et al., 2006). The estimated temperature of mineral formation, 25 °C (95% CI range 21–28 °C), unambiguously identified a summer bias in soil carbonate formation (Fig. 3b).

Given these data, we concluded that soil carbonate dominantly formed during the summer at the time of maximum annual soil moisture and soil CO₂ concentration (Huth, et al., 2019). Formation was largely driven by wet-dry cycles (i.e., infiltration followed by evapotranspiration). While the timing and conditions of soil carbonate formation are clear for the modern setting, the potential exists for soil carbonate formation during other parts of the year, notably in late winter-spring during snowmelt. Therefore, a paleorecord developed at this site requires formation seasonality to be assessed through time in order for viable interpretation.

2.3 Paleorecord and age model construction

The methodology for quantitatively reconstructing $\delta^{18}O_{soil-water}$ and vegetation composition requires coupling modern soil observations, $\delta^{13}C_{sc}$ and $\delta^{18}O_{sc}$ records, and paleotemperature estimates. To that end, the record presented here is composed of radiocarbon dates, two SIMS-based $\delta^{13}C_{sc}$ and $\delta^{18}O_{sc}$ transects, and a $T(\Delta_{47})$ transect. Due to the large amount of material required for these analyses, we

sampled from two different rind pieces. One piece was used to acquire radiocarbon dates and the $T(\Delta_{47})$ transect (Fig. 4) while the other piece was used for the SIMS analyses (SI Appendix, Fig. S3).

2.3.1 Sample resolution considerations

Scanning Electron Microscope (SEM) images of Pendant 11-8 showed significant fine-scale heterogeneity in lamination curvature (over $10s-100s~\mu m$) and, among other structures like silicate grains and void spaces, the presence of $10-100s~\mu m$ diameter carbonate nodules (Fig. 2c). The radiocarbon and Δ_{47} samples were acquired using a MicroMill system and consisted of $300-1200~\mu m$ thick sections of rind. Given the large size of these samples, it is unlikely that fine-scale lamination curvature could significantly bias the data. However, samples would have necessarily incorporated (potentially old) nodules and any reprecipitated/detrital carbonate material. Either of these sources would bias our age model and could affect paleothermometry estimates. Below, we argue against significant contribution from these errors by comparison to other paleorecords and modern soil temperature cycling. For the $\delta^{13}C_{sc}$ and $\delta^{18}O_{sc}$ profiles, we used SIMS to avoid significant time-averaging of the signal (see also SI Appendix). Given the fine analysis spot diameter for SIMS ($10~\mu m$ for $\delta^{18}O$ and $7~\mu m$ for $\delta^{13}C$), we were able to avoid nodules during analysis (Figs. 2c and 4b).

2.3.2 SIMS analyses of $\delta^{13}C_{sc}$ and $\delta^{18}O_{sc}$

We measured $\delta^{13}C_{sc}$ and $\delta^{18}O_{sc}$ values at the University of Wisconsin-Madison WiscSIMS facility (Valley & Kita, 2009; WiscSIMS, 2018; Oerter, et al., 2016). We cut two 1.5 cm wide sections of Pendant 11-8 (SI Appendix Fig. S3) to 4 mm thickness and cast them into a 25 mm diameter epoxy round (Buehler Epo-Thin) along with three grains of UWC-3 calcite standard ($\delta^{18}O = -17.07$ % VPDB, $\delta^{13}C = -0.91$ % VPDB) (Kozdon, et al., 2009). After polishing, the round was sputter-coated with Au to an \approx 60 nm thickness. We identified target transect sites using an optical microscope and the University of Utah Nanofab Lab's FEI Quanta 600F Scanning Electron Microscope at 1,000× magnification in secondary electron mode. We analyzed two transects (T1 and T2) for $\delta^{18}O$ and $\delta^{13}C$ using the large-radius,

multicollector CAMECA IMS 1280 at WiscSIMS following previous studies (Valley & Kita, 2009; Kita, et al., 2009; Williford, et al., 2013). The primary beam ablated 10 μ m (δ^{18} O) or 7 μ m (δ^{13} C) diameter pits to a depth of \approx 1 μ m. The spot-to-spot reproducibility values for the data were determined for the eight UWC-3 standard analyses that bracketed 10–15 sample analyses; average reproducibility was ± 0.2 % (2 SD) for δ^{18} O and ± 0.8 % for δ^{13} C. We defined suitable analysis spots by yield (e.g., δ^{13} C analyses with high relative yield compared to carbonate standards indicate analysis of organic carbon and must therefore be excluded (Tukey, 1977)) and pit quality (e.g., pit shape, presence of cracks and inclusions; SI Appendix Fig. S5; (Wycech, et al., 2018)). In addition, we corrected for Mg content via Electron Microprobe Analysis (Valley & Kita, 2009; Turnier, et al., 2019).

2.3.3 Δ_{47} analyses

We micromilled subsamples of soil carbonate from Pendant 11-8 in 400 μ m lines at the University of Utah (Fig. 4; SI Appendix, Fig. S2). After combining one to three subsamples to acquire appropriate sample size (400–1200 μ m sections for 8–10 mg per replicate), we analyzed samples and standards for Δ_{47} on an automated CO₂ extraction and purification system connected to a ThermoFinnigan MAT 253. We also made sub-daily measurements of CO₂ gases with known δ^{13} C and δ^{18} O values equilibrated at 0 °C and 1,000 °C to observe instrument linearity and to generate an empirical transfer function, which allows for presenting data in an absolute reference frame (Dennis, et al., 2011). Data were corrected for mass interference from ¹⁷O following (Schauer, et al., 2016). For reference, we observed the following Δ_{47} values for carbonate standards analyzed during the same analytical session: NBS-19, 0.389 \pm 0.013 % (1 s, n = 21); HAF Carrara (a.k.a. YCM), 0.383 \pm 0.012 % (n = 19); 102-GC-AZ01, 0.692 \pm 0.013 % (n = 36).

2.3.4 ¹⁴C dating

We milled sections from the rind to obtain approximately 10 mg of sample (SI Appendix, Fig. S2). We extracted CO₂ from samples, purified the gas under vacuum, and graphitized it before AMS and

δ¹³C measurements at the Arizona AMS Laboratory. Samples labeled 14C-2016-0## are from a single transect and were acquired by combining several sub-samples, milled at 100 μm resolution (generally 300 μm sections; SI Appendix, Fig. S2, Table S5). In an attempt to extend the age model past 18 ka, samples TR-04 and TR-05 were milled on the same rind piece, but on a different transect ≈1 cm away from the 14C-2016-0## samples. To minimize the width of sampling footprint and allow the same rind piece to be used for all radiocarbon samples, TR-0# samples were acquired by (1) milling single sections following the diameter of the drill bit and then (2) chipping out the material outlined by the milled sections (SI Appendix, Fig. S2). For age model construction, distance-age correlation was based on distance along the rind for the transect of 14C-2016-0## samples, with TR-0# samples transposed to this transect by following prominent laminations that guided drilling. Their reported boundary and midpoint positions therefore have higher uncertainty than other samples (SI Appendix, Table S5), but the exact positions picked do not affect our interpretation. A dissolution feature identified in the sample constrains the upper age limit of the transect (SI Appendix, Figs. S2 and S3) and we exclude TR-05 from the age model as it may have incorporated some of this material.

2.3.5 Age models for $T(\Delta_{47})$ and SIMS data

We constructed the age model using the Bacon age-modeling software, which utilizes IntCal13 to calculate calibrated radiocarbon ages (Fig. 4; (Blaauw & Christen, 2011; Reimer, et al., 2013)). Radiocarbon samples track the average growth rate of the rind. However, different rind locations had variable growth rate compared to the average rind growth rate (e.g., compare rind pieces in Figs. 2b, 3a, SI Appendix, Figs. S2–S3), which is especially important to assess for SIMS transects considering the fine scale of analysis (<10 µm spots). To account for this variability along individual transects, the age model for the SIMS data was based on linear interpolation between marker laminations that was then tied to the Bacon age model. As a result we use the metric "% through rind" for our age model (Fig. 4c), which can be converted to true distance (i.e., mm from rind edge) for any piece of rind by measuring the distance between marker laminations and the total rind thickness at that point (Fig. 2b, SI Appendix, Fig.

S3, Table S5). Marker laminations for the youngest material (<11 ka) were unambiguous but older marker laminations were not as clear, so we have most confidence in the timing of changes observed for the Holocene. Each SIMS transect was fit with a 1,000-yr window moving average to highlight temporal trends.

In addition to our observation that the two rind pieces share marker laminations, we justify the use of a single age model for both rind pieces by comparing stable isotope transects between the two. We used a laser ablation GC/IRMS system (method of Passey & Cerling, 2006) on the rind piece used for 14 C and Δ_{47} sampling to quickly acquire three coarse-resolution isotope transects (laser analyses required 2-100 µm diameter spots. Data was standardized to a single in-house calcite standard (Laser Marble Std; δ^{18} O = -4.80 % VPDB, δ^{13} C = 1.37 % VPDB) and blank determinations were negligible so we did not apply a blank correction (Passey & Cerling, 2006). Like the SIMS data, the age model for the laser ablation data was based on linear interpolation between marker laminations that was then tied to the Bacon age model. We expected SIMS- and laser ablation-derived data to be offset from one another because of their different standardization routines. In addition, we expected that the coarser spatial resolution of the laser ablation analyses would tend to mute observed isotopic variability as compared to the SIMS data. Even with these constraints, laser ablation-derived and SIMS-derived data largely show the same isotopic patterns, supporting our use of a single age model for both rind pieces (SI Appendix, Fig. S4). We do not interpret the laser ablation-derived transect further, given the coarse resolution of the analyses compared to the SIMS analyses.

In order to highlight temporal trends in $T(\Delta_{47})$, especially where data have single replicates (26–6 ka), we took weighted averages of the data over the following intervals: 0–10, 10–15, 15–20, 20–25, and 25–35 ka. We calculated $T(\Delta_{47})$ using the inorganic calibration of (Defliese, et al., 2015) and provide ranges for one standard error of the mean (SE) and the 95% confidence interval (95% CI) (Fig. 5). Our interpretation is insensitive to choice of calibration and intervals (SI Appendix, Fig. S6, Table S1; (Bonifacie, et al., 2017; Henkes, et al., 2013)).

2.4 Paleoenvironmental reconstruction methodology

2.4.1 Vegetation composition reconstruction (%C₃ plants)

We modeled vegetation composition as the percentage of C_3 plants active on the landscape at the time of mineral formation (% C_3 ; Fig. 6; SI Appendix, Figs. S7 and S8) Forward models exist to predict $\delta^{13}C_{sc}$ from observed $\delta^{13}C_{soil\text{-}CO_2}$ (Cerling, 1984; Davidson, 1995). We used a Monte Carlo approach that combined our knowledge of past environmental conditions in conjunction with the model of (Davidson, 1995) to quantitatively reconstruct past vegetation composition. The process involves three steps: (1) using the range of late Quaternary environmental conditions to model all possible values of $\delta^{13}C_{sc}$, (2) determining the plausible conditions of soil carbonate formation by comparing modeled environmental conditions with known soil conditions, and (3) converting the plausible values of $\delta^{13}C_{soil\text{-respiration}}$ to % C_3 plants on the landscape.

We first created a set of all values of $\delta^{13}C_{se}$ possible under late Quaternary climate conditions. These model values serve as potential matches for the observed data in the second step, where we invert for $\delta^{13}C_{soil\text{-respiration}}$. To create the possible Quaternary values, we modeled $\delta^{13}C_{soil\text{-CO}_2}$ and then converted it to $\delta^{13}C_{se}$. We modeled $\delta^{13}C_{soil\text{-CO}_2}$ using a steady-state system with two CO_2 sources (soil respiration and air) and dominated by diffusive transport (Davidson, 1995). The model uses inputs of soil CO_2 concentration, $\delta^{13}C_{soil\text{-respiration}}$, atmospheric CO_2 concentration, and $\delta^{13}C_{atmospheric\text{-CO}_2}$. We ran 10^7 simulations over a range of values representative of all possible late Quaternary conditions; in other words the entire range of $\delta^{13}C_{soil\text{-respiration}}$ values possible with C_3 and C_4 photosynthesis was included and soil CO_2 was allowed to be as low as atmospheric levels (soil $CO_2 = 150$ –10,000 ppm, $\delta^{13}C_{soil\text{-respiration}} = -10$ to -30 % VPDB, atmosphere $CO_2 = 150$ –300 ppm, and $\delta^{13}C_{atmospheric\text{-CO}_2} = -6$ to -7 % VPDB). We converted the modeled $\delta^{13}C_{soil\text{-CO}_2}$ values to $\delta^{13}C_{se}$ using our paleothermometry estimates in conjunction with a temperature-dependent fractionation factor over the range 10–30 °C (Romanek, et al., 1992).

Second, we determined the model conditions that could plausibly create the moving average $\delta^{13}C_{sc}$ values in order to infer the $\delta^{13}C_{soil\text{-respiration}}$ at the time of sample formation; in other words, we

inverted for $\delta^{13}C_{soil\text{-respiration}}$ using reasonable constraints on variables. This was done by comparing $\delta^{13}C_{sc}$, soil temperature, atmospheric CO₂ concentration, and soil CO₂ concentration of modeled conditions and measured or inferred past conditions. We used our isotopic analyses to constrain $\delta^{13}C_{sc}$ and soil temperature. We required modeled values of $\delta^{13}C$ to be within ± 0.1 % of the moving average $\delta^{13}C$ values. For temperature, each moving average-filtered $\delta^{13}C_{sc}$ datum was assigned a paleotemperature range (SE and 95% CI) based on its age. Modeled soil temperature was required to be within this range.

Atmospheric CO_2 concentration and its $\delta^{13}C$ were matched to gas measurements from polar ice cores within a 500 yr age window (Eggleston et al., 2016; [dataset] Bereiter et al., 2015). This allowed each datum to be matched to at least one set of atmospheric values. A minimum level of variability was set around the mean of all data points that allowed the simulation to proceed in a reasonable number of runs, but that would not significantly influence the results (± 5 ppm for atmospheric CO_2 and ± 0.1 % for $\delta^{13}C_{atmospheric-CO_2}$).

For soil CO₂, constraining its lower boundary was especially important because atmospheric CO₂ is an important contributor to soil CO₂ under near-atmospheric soil CO₂ levels. If soil CO₂ concentration is low, δ^{13} C_{soil-respiration} is difficult to determine because respiration is contributing relatively little to the overall soil CO₂ pool (note that for a set respiration rate, this effect is diminished under lower atmospheric pCO₂ conditions like those of the Last Glacial Maximum). Modern soil carbonate at Torrey forms in summer when annual soil CO₂ is at its highest (3,000–8,000 ppm) and modern soil CO₂ never drops below 1,000 ppm in winter. In addition, our paleothermometry data demonstrate consistent summer formation throughout the record (see *3. Results*). Given these constraints, and even considering a 50% decrease in summer soil CO₂, we argue it is likely that soil CO₂ was always several times atmospheric levels during soil carbonate formation. We therefore used soil CO₂ = 1,000–8,000 ppm to select plausible scenarios for the data set.

Once the plausible scenarios had been identified, we quantified vegetation composition for each data point by converting model values of $\delta^{13}C_{\text{soil-respiration}}$ to %C₃. This conversion was made using a two-

endmember mixing model under the assumption that $\delta^{13}C_{\text{soil-respiration}}$, and thus $\delta^{13}C_{\text{sc}}$, is largely derived from near-contemporaneous plant material. Choice of the C_3 and C_4 endmember values was important because the difference between $\delta^{13}C_{\text{plant}}$ and $\delta^{13}C_{\text{atmospheric-CO}_2}$ (the source signal for plants) can also be a function of other variables (Ehleringer & Monson, 1993). The value of the C_3 endmember may be estimated, in conjunction with known pCO₂ and $\delta^{13}C_{\text{atmospheric-CO}_2}$ conditions, as a function of water stress or atmospheric CO₂ concentration (e.g., (Schubert & Jahren, 2012; Schubert & Jahren, 2018; Breecker, et al., 2012; Breecker, 2017; Hare, et al., 2018; Diefendorf, et al., 2010; Kohn, 2010; Kohn, 2016; Bowling, et al., 2002)), so we allowed a range of values based on these calibrations.

For the CO₂ concentration effect, we considered the multiple species calibration of Schubert and Jahren (2012; their Eqn. 6), which can be applied to each data point based on the CO₂ concentration and $\delta^{13}C_{atmospheric-CO_2}$ conditions inferred from ice core records. The overall calculated range of the $\delta^{13}C$ value of C₃ endmember as a function of atmospheric CO₂ concentration was -25.6 to -22.9 % VPDB (SI Appendix, Fig. S8).

For the water stress effect, we considered the calibrations of Diefendorf et al. (2010) and Kohn (2010). Both calibrations are primarily functions of mean annual precipitation (MAP), but also utilize secondary parameters. We followed the authors' apparent or stated preferred calibrations; Diefendorf et al. (2010) also considers altitude (global relationship in their Supporting Information, pg. 3) and Kohn (2010) also considers altitude and latitude (their Eqn. 2). We considered an MAP range of 130–1040 mm/yr (i.e., 0.5–4× modern MAP) as a range likely to cover that experienced at Torrey, UT over 0–35 ka (e.g., Marchetti et al., 2011; Oster et al., 2015; Anderson et al., 2000). This range also uses modern elevation-climate relationships as an analog for LGM climate. During the LGM, plants had elevational depressions of 100s–1000 m below present day locations (Anderson, et al., 2000). Modern MAP in the highlands near Torrey, which are 800–1000 m higher, have MAP ranges of 600–900 mm/yr and mean annual temperature values that are ≥ 7 °C cooler (Horel, et al., 2020; Prism Climate Group, 2018). While a simple elevation-based translation of modern climate is not a perfect analog, we use it as a reasonable

estimate of the magnitude of change in lieu of past MAP estimates. As with the CO_2 concentration calibration, we included the range of $\delta^{13}C_{atmospheric-CO_2}$ conditions inferred from ice core records over 0–35 ka.

The overall calculated δ^{13} C range of the C_3 endmember for both types of calibrations combined was -24.3 to -21.4 % VPDB (see SI Appendix, Fig. S8 for plots using individual calibrations). We set the δ^{13} C value for the C_4 endmember to -10 % VPDB based on the average isotopic compositions of preindustrial plants following the C_4 photosynthetic pathways and the effects of water stress on plant δ^{13} C values (Cerling & Harris, 1999; Tipple & Pagani, 2007).

$2.4.2 \, \delta^{18} O_{\text{soil-water}}$ reconstruction

The distribution of isotopes between two phases in equilibrium, here soil carbonate and soil water, can be described by a temperature-dependent fractionation factor. We thus modeled $\delta^{18}O_{\text{soil-water}}$ by using the moving average-filtered $\delta^{18}O_{\text{sc}}$ profiles and paleothermometry estimates (Fig. 7). We assigned each $\delta^{18}O_{\text{sc}}$ datum a paleotemperature range (SE and 95% CI) based on its age. The relevant temperature-dependent fractionation factors were calculated for each point (Kim & O'Neil, 1997) and used to model the range of $\delta^{18}O_{\text{soil-water}}$ values consistent with the data. Other calibrations for the fractionation factor are possible (Coplen, 2007; Affek & Zaarur, 2014), but note that the similar temperature sensitivity of all three calibrations necessarily produces similar patterns of reconstructed $\delta^{18}O_{\text{soil-water}}$ (SI Appendix Fig. S9). However, use of the Coplen (2007) calibration will shift data more negative by \approx 1.5 % and use of the Affek & Zaarur (2014) calibration will shift data more negative by \approx 1 % and result in more muted patterns due to a smaller temperature sensitivity than the other calibrations. Therefore, while we present the reconstruction using the Kim & O'Neil (1997) calibration, we emphasize that patterns of change are the most robust aspect of the $\delta^{18}O_{\text{soil-water}}$ reconstruction. Beyond calibration choice, the large 5–10 ka intervals used to average T(Δ_{47}) are the biggest source of error in our approach. This error can likely be

minimized by finer spatial sampling enabled by smaller analysis size than was available at the time of this study (\approx 10 mg/replicate vs. <3 mg/replicate).

3 Results

3.1 Age model and paleothermometry

Calibrated radiocarbon dates for Pendant 11-8 were in stratigraphic order and the age model spanned 35–5 ka (Fig. 4). Reconstructed soil temperatures during rind formation were ≈18 °C during the Last Glacial Maximum (LGM, 25–20 ka) and 20–25 °C at other times (Fig. 5c).

3.2 $\delta^{13}C_{sc}$ and reconstructed %C₃ plants

The $\delta^{13}C_{sc}$ transects spanned 35–5 ka and largely agree in pattern (Fig. 5a). From 35–10 ka, $\delta^{13}C_{sc}$ was fairly constant between -2 to -4 % VPDB. However, during the Holocene it spanned a large, 10 % range. Values of $\delta^{13}C_{sc}$ data were lower from 9–7 ka at -4 to -6 % VPDB, and starting at 7 ka they increased towards the present until they reached their highest values, +3 % VPDB, at 5 ka.

Reconstructed vegetation composition follows these same trends, with the highest inferred $\%C_3$ plants corresponding to the lowest $\delta^{13}C_{sc}$ values (Fig. 6). The $\%C_3$ plants ranged from 0–100 $\%C_3$ plants for the -21.4 % VPDB endmember and 0–75 $\%C_3$ plants for the -26.7 % VPDB endmember. During the last glacial period, the vegetation generally consisted of 30–90 $\%C_3$ plants, which increased to a maximum of 45–100 $\%C_3$ plants during the Early Holocene. This was followed by a large decline in C_3 plants starting at 7 ka. By 3 ka, we model 0–10 $\%C_3$ plants on the landscape.

3.3 $\delta^{18}O_{sc}$ and reconstructed $\delta^{18}O_{soil-water}$

The $\delta^{18}O_{sc}$ transects show the same general patterns, but significant discrepancies between the transects exist, notably from 12–8 ka (Fig. 5b). Discrepancies are potentially derived from issues with the age model, difficulty obtaining suitable analysis spots, data density (especially >15 ka), and/or small scale variability in $\delta^{18}O_{soil-water}$ at the time of mineral formation (e.g., (Gazis & Feng, 2004; Treadwell-Steitz &

McFadden, 2000; Sprenger, et al., 2016)). From 31–9 ka, $\delta^{18}O_{sc}$ ranged from -9 to -12 ‰ VPDB where analysis spots were most concentrated. The transects differ by up to 1.5 ‰ from 12–10 ka, although note the limited analysis spots in this time slice. Transect 1 increases from -11 to -9 ‰ VPDB between 11–9 ka and then decreases to -11 ‰ VPDB by 8 ka. Transect 2 may show a similar trend, but identifying trends at this time is difficult because it is not clear if the variability between successive data points is real or an issue with the age model or SIMS analysis (see also SI Appendix, Fig. S5). The transects show good agreement for the remainder of the record. From 8–6 ka, both transects increase to -8 ‰ VPDB and then decrease slightly to -9 ‰ VPDB at the end of the record.

Reconstructed $\delta^{18}O_{soil\text{-water}}$ ranged from -11 to -6 ‰ VSMOW, varying between the full range of modern observed $\delta^{18}O_{soil\text{-water}}$ values (Fig. 7). The largest difference in pattern between $\delta^{18}O_{soil\text{-water}}$ and $\delta^{18}O_{sc}$ is at 25–20 ka. Between 25–20 ka, $\delta^{18}O_{soil\text{-water}}$ is -11 to -10 ‰ VSMOW, and then increases during deglaciation to -9 to -8 ‰ VSMOW. In contrast, $\delta^{18}O_{sc}$ remains fairly constant through time. This difference is driven by the change in formation temperature between 25–20 ka (Fig. 5c). At all other times, $\delta^{18}O_{soil\text{-water}}$ generally follows the same pattern as $\delta^{18}O_{sc}$. The two $\delta^{18}O_{soil\text{-water}}$ transects are in disagreement by up to 2 ‰ between 12–9 ka, but then both increase to -9 ‰ VSMOW by 8 ka. Between 8–4 ka, both transects showed $\delta^{18}O_{soil\text{-water}}$ increasing from -9 to -6 ‰ VSMOW, and then decreasing slightly to -7.5 ‰ VSMOW at the end of the record.

4 Discussion

4.1 Late Quaternary climate and vegetation change in Torrey, UT

4.1.1 Soil carbonate formation conditions inferred through time

Reconstructed soil temperature over the last 40 ka most likely reflects summer soil temperature. The temperature increase from the LGM to the Holocene of ≈7 °C is consistent with previous inferences of regional change (Fig. 5). For example, Marchetti et al. (2011) used terminal and recessional moraines on the nearby Boulder and Fish Lake Mountains (dated to 23–19 ka and 16–14 ka respectively) to estimate summer temperature depression as compared to modern (Fig. 7). Our estimate of summer soil

temperature depression between the Holocene and LGM is similar to or smaller than their estimates for summer temperature depression for the >2700 m Fish Lake Plateau depending on precipitation amount (- 10.7 to -8.2 °C for LGM precipitation = $1 \times$ modern, -6.7 to -9.2 °C for LGM precipitation = $1.5 \times$ modern; (Marchetti, et al., 2011)).

The continuously warm soil temperature data support interpreting the $\delta^{13}C_{sc}$ and $\delta^{18}O_{sc}$ data in the context of our modern calibration study where soil carbonate forms in the warmest summer months (Fig. 3). Significant summer rainfall must have always occurred in the last 40 ka to allow soil carbonate to consistently form in the summer. A shift to a different regime of rainfall seasonality would require soil carbonate to form at a different time of year and reconstructed soil temperature would accordingly not be uniquely consistent with summer values. This validates our approach in modeling $\delta^{13}C_{sc}$ and $\delta^{18}O_{sc}$ as the %C₃ plants and $\delta^{18}O_{soil-water}$, respectively, that are present during summer (as opposed to mean annual conditions). Within this framework, we note the most negative reconstructed $\delta^{18}O_{soil-water}$ values (-11 to - 12 % VSMOW; Fig. 7; SI Appendix, Fig. S9) are well outside the modern observed summer range; we explore explanations for this observation below.

4.1.2 Climate and vegetation composition during the last glacial period

We discern broad trends in our record during the last glacial period but we ignore millenial-scale variability during this time period as data density and age control are imprecise. During the last glacial period model estimates generally show a mix of C₃ and C₄ plants existed on the landscape (30–90 %C₃ Fig. 6), although note that the wide constraints on the C₃ endmember value preclude a precise estimate. However, climate during the last glacial period in the western USA was cooler and may have had increased effective moisture, as evidenced by the greater extent of lakes, glacial advances, and shifts in vegetation boundaries by latitude and elevation (Marchetti, et al., 2011; Coats, et al., 2008; Madsen, et al., 2001; Anderson, et al., 2000). This suggests that scenarios using more negative C₃ endmember values, associated with a larger C₄ plant proportion, are probably most likely. Our interpretation is consistent with other regional records suggesting that C₄ plants persisted through the last glacial period (Cole & Monger,

1994; Liu, et al., 1996), with the implication that climate conditions were generally suitable for C₄ plants due to lower atmospheric CO₂ concentration accompanied by warm season rainfall (Ehleringer, et al., 1997).

The overall decrease in $\delta^{18}O_{soil-water}$ at the LGM and then increase during deglaciation could have been driven by changes in the air temperature during rainfall, infiltration seasonality, evaporation intensity, and/or source water (Fig. 7). The NAM may derive water from both the Gulf of Mexico and the Gulf of California, which could produce ≈ 1 ‰ variability in our record (Schmidt, et al., 1999) and changes in winter source water could cause several per mil variability (Lachniet, et al., 2014). Increasing air temperature by ≈ 7 °C from 25–10 ka could also have driven a substantial portion of the overall increase in $\delta^{18}O_{soil-water}$ via changes in $\delta^{18}O_{rain}$ and $\delta^{18}O_{snow}$. Likewise, as the region warmed during this time period, increasing evaporation intensity could have driven increasing $\delta^{18}O_{soil-water}$. Changing the proportion of seasonal infiltration could also cause a comparable increase in $\delta^{18}O_{soil-water}$.

While disentangling these effects is difficult in a single record, our $\delta^{18}O_{soil\text{-water}}$ data are consistent with interpretations from other climate records. Cooler temperature during meteoric precipitation events and decreased soil evaporation would both act to decrease $\delta^{18}O_{soil\text{-water}}$ values in the LGM portion of the record. Then, as temperature (and soil evaporation) increased during the deglaciation, $\delta^{18}O_{soil\text{-water}}$ values would have correspondingly increased. Increased moisture delivery or changing moisture source region during winter at the LGM is also consistent with the Torrey $\delta^{18}O_{soil\text{-water}}$ reconstruction (Oster, et al., 2015; Lachniet, et al., 2014).

4.1.3 Climate and vegetation composition during the Holocene

The greater data density and age control in the Holocene portion of the Torrey record allow for more detailed interpretation and record comparison. We infer that vegetation underwent a dramatic shift from the Early to Middle Holocene (Fig. 6). Between 10–7 ka, C_3 plants dominated the landscape, reaching their greatest abundance between 7 and 9 ka (45–100 % C_3). After this point, C_3 plants declined until they were essentially absent on the landscape by 5 ka (<10 % C_3). Note that $\delta^{13}C_{sc}$ at 5 ka is so

positive that our interpreted decline is robust to even C₃ endmember values of -30 ‰ VPDB. As part of this interpretation, we infer that the $\approx 10 \% \delta^{13}C_{sc}$ shift from 7–5 ka was caused by an increase in C₄ vegetation and not a decline in overall summer respiration (Cerling, 1984). Three lines of evidence support this inference. First, consistent formation of soil carbonate in the summer throughout the Holocene requires summer rainfall be an important contributor to annual rainfall (Huth, et al., 2019). Second, if the highest $\delta^{13}C_{sc}$ values (+3 % VPDB) were created in a mixed C_3 - C_4 environment similar to modern (≈50 %C₃), soil respiration would have to be reduced by >99%. Modern soil pCO₂ values consistent with such low respiration are not observed even in mid-winter at Torrey (≈1,000 ppm CO₂; Fig. 3). Additionally, the required dry annual conditions would be more consistent with soil carbonate formation at the soil surface and not at 40 cm depth. Third, a local packrat midden sequence from nearby Hartnet Draw in Capitol Reef National Park (1920 masl, 25 km from Torrey; Fig. 1) supports the inference of significant respiration from vegetation growing during the summer. The Hartnet Draw midden sequence documented a significant grass and shrub component at 5.4 ka, which the authors interpreted as a relatively stable vegetation regime until the advent of intensive grazing in the 1800s (Cole, et al., 1997). However, packrat middens are, like all proxies, imperfect recorders and are thought to quantitatively underestimate the abundance of grasses on the landscape (Betancourt, et al., 1990). When combined with our soil carbonate record, it is clear that while the overall landscape may have been consistently dominated by shrubs and grasses through the Mid- to Late-Holocene, significant changes in the favored plant photosynthetic pathway occurred.

489

490

491

492

493

494

495

496

497

498

499

500

501

502

503

504

505

506

507

508

509

510

511

512

513

514

We interpret the Holocene δ¹⁸O_{soil-water} data in the context of the %C₃ record (Fig. 7). In regions with summer rainfall regimes, C₄ plants generally outcompete C₃ plants under higher summer temperature conditions (Ehleringer & Monson, 1993; Ehleringer, et al., 1997; Holmgren, et al., 2007; but see also, e.g., Cole and Monger, 1994); such relationships have been demonstrated over large geographic and altitudinal ranges (Ehleringer, et al., 1997; Nordt, et al., 2007; Teeri, et al., 1980; Teeri & Stowe, 1976; Wentworth, 1983). Because these relationships have historically been developed in the context of plant abundance within a flora they do not explicitly account for seasonal productivity. This is an important

consideration in the context of the summer-biased Torrey record as temporal separation in C₃-C₄ plant activity has been documented in similar semi-arid environments (e.g., Kemp, 1983; but see also Bowling et al., 2011). We therefore stress that the Torrey paleovegetation reconstruction provides information about *summer* conditions and correspondingly may only provide a minimum estimate of mean annual %C₃ (i.e., C₃ plant abundance within a flora). In addition, we recognize that complicating situations exist where the predicted relationship between increased temperature and the abundance of C₄ plants does not hold (e.g., (Cole & Monger, 1994)).

515

516

517

518

519

520

521

522

523

524

525

526

527

528

529

530

531

532

533

534

535

536

537

538

539

540

Regardless of these other effects, temperature is likely still an important control on \(\%C_3 \) plants and we subsequently use this relationship as one pathway to interpret the Holocene $\delta^{18}O_{\text{soil-water}}$ interpretation. In the context of the above seasonal bias considerations, the scale of temperature change required to produce large apparent %C₃ changes (Fig. 6) should be less than required by modern continental-scale calibrations (a few degrees Celsius vs. ≈10 °C). Note that because our reconstructed temperature data have coarse temporal resolution and, in general, have few replicates, this dataset cannot be used to directly identify Holocene temperature change. Nonetheless, from the start of the Holocene to 7 ka we infer relatively cool conditions must have existed to support a summer landscape composed dominantly of C₃ plants (Ehleringer, et al., 1997). During this period of relative vegetation stability, summer δ¹⁸O_{soil-water} values varied by 3 % VSMOW. We cannot explicitly rule out changes in air temperature or evaporation intensity and their effects on $\delta^{18}O_{\text{soil-water}}$. However, if air temperature (and by association evaporation intensity) varied significantly throughout this interval, %C₃ values should not have maintained a relatively narrow range. Changing summer source water could potentially explain ≈1 ‰ of the variability, but such changes are not inferred to occur until the Mid-Holocene (Barron, et al., 2012); in any event this is not a sufficient isotopic driver. Instead, changes in winter source water (e.g., (Lachniet, et al., 2014)) and/or the relative proportion of seasonal infiltration are more likely drivers. Each winter, snowmelt "resets" $\delta^{18}O_{\text{soil-water}}$ to a baseline value, which today is several per mil higher than $\delta^{18}O_{snow}$ (Fig. 3). Then, over the course of the summer, $\delta^{18}O_{soil-water}$ is driven to higher values as a result of summer rainfall and evaporation (Huth et al., 2019). By having more winter infiltration or infiltrating

water with lower $\delta^{18}O$, the springtime baseline $\delta^{18}O_{\text{soil-water}}$ could be lowered and summer $\delta^{18}O_{\text{soil-water}}$ values could be significantly altered.

We therefore interpret the Early Holocene $\delta^{18}O_{soil-water}$ data in the context of source water and infiltration. In the earliest Holocene, increased winter infiltration or a more northerly moisture source created lower $\delta^{18}O_{soil-water}$. Then, the soil system began to receive relatively less winter infiltration, or moisture from a more southerly source, reaching a local maximum in $\delta^{18}O_{soil-water}$ values around 8 ka. Lower $\delta^{18}O_{soil-water}$ conditions were established towards 7 ka via more winter infiltration or water from a more northerly source. From 7–5 ka, C_3 plants on the landscape were replaced by C_4 vegetation (Fig. 6), suggesting increasing temperature began to play an important role in soil water cycling along with infiltration seasonality and moisture source. Increasing evaporation intensity driven by higher summer temperature may therefore have caused the increase in $\delta^{18}O_{soil-water}$ from 7–6 ka. The final recorded decrease in $\delta^{18}O_{soil-water}$ from 6–5 ka occurred as C_3 plants continued to decline. The continued decline in C_3 plants is consistent with increasingly warm summer conditions, which makes it unlikely that evaporation intensity would have lessened at this time. Instead, we infer that the decrease in $\delta^{18}O_{soil-water}$ was driven either by increased winter infiltration or a moisture source with a lower $\delta^{18}O$ value.

Paleorecords developed from lakes and wetlands near Torrey support a combination of infiltration seasonality and evaporation intensity as primary drivers of $\delta^{18}O_{soil-water}$ change but do not speak to seasonal moisture sources (Fig. 1). On the basis of pollen ratios for plants with different hydrologic niches, the authors of these studies qualitatively inferred changes in local hydrology through time. Two mid-elevation records from Garden Basin Cattail Fen (\approx 2400 masl) and Posy Lake (2646 masl) document high Early Holocene annual moisture decreasing between 8–7 ka and 5–4 ka, respectively, due to decreased summer moisture (Morris, et al., 2013; Shurtliff, et al., 2017) with increasing moisture occurring in the Late Holocene. In addition, inferred treeline elevation increased between the Early and Mid-Holocene, which suggests increasing temperature at this time. Discrepancies in the timing of inferred vegetation and climate change between these records could be due to real variability in this topographically complex region (Barron, et al., 2012; Metcalfe, et al., 2015) but could also be related to

comparing different record types with different sample resolution. Nonetheless, it is reasonable to infer that $\delta^{18}O_{\text{soil-water}}$ was driven by increased aridity between the Early and Mid-Holocene due to a combination of decreased summer rainfall and higher temperature.

It is noteworthy that all of these records suggest that changes in vegetation occurred in concert with increasing summer aridity. However, despite increased summer aridity between the Early and Mid-Holocene, a summer rainfall regime must have persisted to support C_4 vegetation. We recognize that the present $\delta^{18}O_{\text{soil-water}}$ dataset cannot be unambiguously parsed into individual effects from rainfall temperature, evaporation intensity, infiltration seasonality, and/or moisture source. We therefore cannot fully understand the complex relationships between changes in vegetation structure due to temperature, rainfall, soil aridity, and other drivers. However, the potential exists to assess individual $\delta^{18}O_{\text{soil-water}}$ drivers using soil carbonate rinds and test relationships between environmental conditions and dominant plant photosynthetic pathway through time (see 4.3.3. Avenues for exploration).

4.2 Coherent connections to the western USA and Mexico

Our interpretation is generally consistent with changes in western USA climate and vegetation interpreted from other records. For example, low elevation records in the Great Basin have been interpreted as indicative of warm and/or wet conditions in the Early Holocene changing to drying and/or warming conditions in the Early- to Mid-Holocene (e.g., (Steponaitis, et al., 2015; Schuman & Serravezza, 2017)). These climate changes were accompanied by vegetation changes; xeric species replaced more mesic ones from ≈13–4 ka, but wetter conditions in the last few millennia apparently supported more mesic plants and increasingly freshwater aquatic communities (Madsen, et al., 2001; Schmitt & Lupo, 2012). Similarly, on the Colorado Plateau, Early Holocene forests had expanded ranges associated with wet conditions and a transition to drier summers occurred between 8.6–6 ka (Coats, et al., 2008; Morris, et al., 2013; Metcalfe, et al., 2015). Wetter conditions resumed during the Mid- to Late Holocene, with records documenting increasing water availability between 6.5–4.4 ka.

Regions affected by the NAM show spatial coherence during the Holocene (Metcalfe, et al., 2015) and the Torrey record's apparent inverse correlation with more southerly records is a useful indication that it is linked to larger NAM dynamics. For example, in southern New Mexico, vegetation composition (%C₃) was inferred from a sequence of buried soils containing pedogenic carbonate (Cole & Monger, 1994; Monger, et al., 1998). Although the time resolution of this record is accordingly constrained to the resolution of individual soil units, the authors inferred that vegetation switched from a dominantly C_4 to a dominantly C_3 landscape starting around 9–7 ka (from $\approx 10-30$ % C_3 to $\approx 60-80$ % C_3). Similar trends were inferred between the LGM and Holocene (from ≈40–50 %C₃ to ≈80–90 %C₃) from soils in southern Arizona (Liu, et al., 1996). These switches occur at approximately the same time, but are opposite in direction, to our inferred onset of %C₃ decline in Torrey (Fig. 6). However, note that at both of these study sites C₃-dominated plant communities (desert scrub) occupy warmer, lower elevation sites than C₄-dominated communities (grasslands). Therefore, while the inferred changes in %C₃ between these sites and Torrey are opposite in direction, they may actually represent a coherent response to temperature perturbation (Liu, et al., 1996). Thus, in addition to the timing of change, the opposite direction of signals supports the idea that regional vegetation drivers, like temperature, can override global drivers, like CO₂, in determining western USA vegetation composition (Liu, et al., 1996; Ehleringer & Monson, 1993; Holmgren, et al., 2007; Morris, et al., 2013; Schmitt & Lupo, 2012).

592

593

594

595

596

597

598

599

600

601

602

603

604

605

606

607

608

609

610

611

612

613

614

615

616

Torrey $\delta^{18}O_{soil\text{-water}}$ also correlates with Holocene hydrologic records. For example, Torrey $\delta^{18}O_{soil\text{-water}}$ inversely correlates with the $\delta^{18}O_{speleothem}$ record from Pink Panther Cave, southern New Mexico, which has been argued to be related to the strength of the NAM or the location of its moisture sources (Fig. 7; (Asmerom, et al., 2007; Barron, et al., 2012)). It also inversely correlates with USA Rocky Mountain lake levels (region defined as 30–47.5 °N, 105–112.5 °W; (Schuman & Serravezza, 2017). While the exact interpretation of $\delta^{18}O_{soil\text{-water}}$, $\delta^{18}O_{speleothem}$, and lake level changes is complex, the correlation between all records supports our interpretation of connections between Torrey soil carbonate and wider western USA hydrologic change.

It is not our goal here to disentangle the intricate climate connections between different sub-regions of the western USA with a single record (Barron, et al., 2012; Metcalfe, et al., 2015; Schuman & Serravezza, 2017). Rather, we note that our independent climate and vegetation reconstruction is consistent with local records and that the observed inverse correlations between our southern Utah soil carbonate record and other regional records speak to the more general teleconnections inferred for sites in the western USA during the Holocene. Thus, we conclude that laminated soil carbonate records can be used to reconstruct paleoclimate and paleovegetation.

4.3 The soil carbonate paleoarchive

The utility of laminated soil carbonate rinds to provide continuous paleoclimate and vegetation information has broad implications. The key strengths of this methodology are in (1) its dateable stratigraphy that allows for continuous records, (2) the long record length (10–100s kyr), (3) the prevalence of soil carbonate rinds in the arid and semi-arid regions that cover \approx 30% of Earth's surface, (4) acquiring vegetation ($\delta^{13}C_{sc}$) and climate ($\delta^{18}O_{sc}$) information from a single, internally consistent record, and (5) the immediate connection between soil conditions and overriding climate and vegetation, which is enabled by the record's short hydrologic flow path (\approx 1-m² footprint). Laminated soil carbonate rinds thus offer a way to provide new soils perspectives and supplement existing paleoclimate information. In this final section we outline the key strengths of the laminated rind methodology compared to traditional soil carbonate analysis methods, propose ways to improve the laminated rind methodology, and end with a discussion of future avenues of exploration using laminated soil carbonate rinds.

4.3.1 Improved analysis and interpretation of rinds

Studies making use of the laminated soil carbonate proxy thus far have documented several issues that should be addressed to allow robust interpretation. In the field, samples should be selected for the specific question at hand. In general, this will mean that samples should be collected from a single depth

within a stable deposit to allow for inter-sample comparison, minimize the influence of atmospheric CO_2 on $\delta^{13}C_{soil\text{-}CO_2}$ (Cerling, 1984), and mitigate the effect of evaporation on $\delta^{18}O_{soil\text{-water}}$ (e.g., (Oerter & Amundson, 2016; Huth, et al., 2019; Breecker, et al., 2009)). Modern calibration studies investigating, for example, the annual changes in soil respiration, soil moisture, soil temperature, $\delta^{13}C_{soil\text{-respiration}}$, and $\delta^{18}O_{soil\text{-water}}$ should be conducted to understand when modern soil carbonate forms and what conditions might potentially have existed in the past. These can be combined with soil temperature reconstructions to constrain the timing of soil carbonate formation throughout the length of a record, which is foundational to quantitatively reconstructing vegetation regimes and $\delta^{18}O_{soil\text{-water}}$.

For paleorecord construction, future studies should focus on the scale of sampling, finer-scale age models, and replication. For stable isotope analysis, studies should take advantage of the extremely small spatial resolution of SIMS analyses (\approx 10 µm diameter \times 1 µm deep). While the rind used in this study was >1 cm in length, other rinds record 10–100s ka of environmental change over a mm scale (Oerter, et al., 2016; Pustovoytov, et al., 2007). Micromilling subsamples for analysis can severely dampen the true signal and should only be used for preliminary screening. To acquire finer-scale samples for dating, studies can use laser ablation U/Th methodologies where feasible (Oerter, et al., 2016). Additionally, finer-scale sampling for radiocarbon dating should also be achievable as \approx 1-mg analyses are now possible (Bard, et al., 2015). Finally, replication of records from different rinds at a single site (i.e., same soil, depth, and age range but different locations) has not yet been robustly tested to our knowledge (this study, (Oerter, et al., 2016; Pustovoytov, et al., 2007)). Future studies that constrain the variability within single soils will make the resulting paleoclimate reconstructions more reliable.

4.3.2 Avenues for exploration

Because soil carbonate is common throughout arid and semi-arid soil profiles, the laminated rind methodology presents new avenues for paleoclimate exploration. Studies can now investigate specific landforms of interest (terraces, debris flows, alluvial fans, etc.) which were previously challenging to

investigate except by records that were less continuous and/or suffered from time-averaging issues (e.g., packrat middens, bulk soil samples). In addition to assessing the effect of slope, aspect, and topography on vegetation change within a single overarching climate regime, archeologists can use laminated soil carbonate rinds to reconstruct soil conditions at ancient human occupation sites (Pustovoytov, et al., 2007). Because soil carbonate rinds are common and result from an extremely small flowpath ($\approx 1 \text{-m}^2$ footprint), it should be feasible to directly compare this single record type in regional sequences, for example across the western USA. It should also be possible to test for elevation-dependent response to climate change by analyzing a sequence of soil carbonate rinds along an elevation transect. As demonstrated in this study, the intensity of soil evaporation is likely to be a significant contributor to $\delta^{18}O_{sc}$ and therefore reconstructed $\delta^{18}O_{soil\text{-water}}$. Future studies should test the possibility of reconstructing profiles of $\delta^{18}O_{\text{soil-water}}$, and thus constrain evaporative intensity, by comparing several soil carbonate rind records from different soil depths at a single site. Assessing moisture conditions might also be possible via triple oxygen isotopes (Δ^{17} O) or examining elemental ratios of soil carbonate and its included material through time in a single rind (Passey, et al., 2014). Finally, by selecting soil carbonate rinds from deeper depths, it may be possible to reconstruct mean annual air temperature through time (Harris & Chapman, 1997).

668

669

670

671

672

673

674

675

676

677

678

679

680

681

682

683

684

685

686

687

688

689

690

691

692

In addition to the possibilities for climate and vegetation reconstruction from soil carbonate rinds alone, combining this record type with other records can help to create more complete histories. For example, fossil records (pollen in lake cores, packrat middens) can be discontinuous and, in some cases, underestimate the abundance of vegetation (Betancourt, et al., 1990). By combining fossil vegetation reconstructions with the overall landscape vegetation composition (%C₃) available from soil carbonate records, it should be possible to create detailed, continuous reconstructions of vegetation and vegetation change through time (Cole & Monger, 1994; Liu, et al., 1996). Paleovegetation reconstruction from rind $\delta^{13}C_{sc}$ may also be improved by adding information from included organic matter (i.e., $\delta^{13}C_{organic-matter}$) and phytoliths (Cerling, 1984; Hyland, et al., 2019).

Soil carbonate rinds may also provide complementary information to speleothem data. For example, one source of C in speleothems is soil-respired CO₂, but δ^{13} C_{speleothem} data is rarely used to reconstruct δ^{13} C_{vegetation}. This is because along its flow path to eventual speleothem formation, the δ^{13} C composition of dissolved inorganic carbon can be modified by many processes (e.g., water-rock interactions and kinetic processes during degassing). Records of $\delta^{18}O_{\text{speleothem}}$ records are generally interpreted as largely resulting from climate signals, but demonstrating minimal kinetic effects can be difficult (e.g., (Dorale & Liu, 2009)). In contrast, soil carbonate records are generally regarded to be minimally influenced by kinetic processes during formation (Cerling, 1984). Therefore, assessing high-resolution speleothem isotope data (often <10 yr/sample) in the context of a nearby soil carbonate record might allow assessment of kinetic effects on $\delta^{13}C_{\text{speleothem}}$ through time. In turn, because $\delta^{18}O_{sneleothem}$ records can be less sensitive to evaporation than $\delta^{18}O_{sc}$ records, complementary datasets might be used to assess the effect of climate change on vegetation regimes at a single site. Finally, the sensitivity of each proxy is an important consideration. Even where $\delta^{13}C_{\text{speleothem}}$ data is not unduly influenced by kinetic effects, such records may not respond to changes in C₄ plant abundance due to differences in C₃-C₄ plant rooting depth (Breecker, et al., 2012). In such cases, soil carbonate records will inherently provide a more robust dataset for reconstructing paleovegetation changes.

Conclusion

As demonstrated at a site in Torrey, southern Utah, the emerging laminated soil carbonate proxy provides a record of climate and vegetation changes over 10s ka. Interpreted vegetation (%C₃ plants) and hydrologic ($\delta^{18}O_{soil-water}$) changes agree with interpretations from local pollen records. In addition, the Torrey records correlate with other regional records of vegetation and hydrologic change, demonstrating spatial patterns in line with those previously inferred for the western USA and wider North American Monsoon region (Barron, et al., 2012; Metcalfe, et al., 2015; Schuman & Serravezza, 2017). We conclude that 10–100s kyr of continuous soil information (%C₃ plants and $\delta^{18}O_{soil-water}$) can be independently discerned from soil carbonate records if (1) soil system information is available to constrain the modern

conditions of soil carbonate formation and (2) the conditions of soil carbonate formation can be constrained through time. Enhanced analytical capabilities related to fine-scale isotope composition sampling will enable more detailed datasets with better age models and will improve interpretations. The laminated soil carbonate proxy presents opportunities for geologists, ecologists, soil scientists, and archeologists to assess the development and interactions of landforms, vegetation, climate, and humans over 10s–100s ka in sites that are currently underconstrained or that were previously unfeasible for paleorecord development.

Acknowledgements

The authors thank Jay Quade for the use of his CO₂ extraction and graphitization line. TEH thanks Julia Kelson for applying the ¹⁷O correction to clumped isotope data. This work made use of University of Utah Shared facilities of the Surface Analysis and Nanoscale Imaging group sponsored by the College of Engineering, Health Sciences Center, Office of the Vice President for Research, and the Utah Science Technology and Research (USTAR) Initiative of the State of Utah. **Funding.** This work was supported by NSF grants (EAR 1325214 and 1325225) to TEC, DWM, and ALE and by the following sources to TEH: NSF grant EF 1137336, University of Utah Geology and Geophysics grants, a University of Utah Global Change and Sustainability Center grant, and funds from the University of Utah Geochemistry Laboratory. A GSA Gladys W. Cole award to DWM partially supported this research. WiscSIMS is supported by NSF (EAR-1658823) and the University of Wisconsin. JWV is funded by DOE, Office of Basic Energy Sciences, Geosciences Division (DE-FG02-93ER14389). **Competing interests.** The authors declare no competing interests. **Data and materials availability.** All data are available in the SI Appendix. Samples are housed at the University of Utah and available upon request.

- Affek, H. P. & Zaarur, S., 2014. Kinetic isotope effect in CO₂ degassing: Insight from clumped and oxygen isotopes
- in laboratory precipitation experiments. *Geochimica et Cosmochimica Acta*, Volume 143, pp. 319-330.
- Anderson, R. S. et al., 2000. Middle- and late-Wisconsin paleobotanic and paleoclimatic records from the southern
- 747 Colorado Plateau, USA. Palaeo, Volume 155, pp. 31-57.
- Asmerom, Y., Polyak, V., Burns, S. & Rassmussen, J., 2007. Solar forcing of Holocene climate: New insights from
- a speleothem record, southwestern United States. *Geology*, Volume 35, pp. 1-4.
- Bard, E. et al., 2015. AixMICADAS, the accelerator mass spectrometer dedicated to ¹⁴C recently installed in Aix-
- 751 en-Provence, France. Nuclear Instruments and Methods in Physics Research B, Volume 361, pp. 80-86.
- Barron, J. A., Metcalfe, S. E. & Addison, J. A., 2012. Response of the North American monsoon to regional changes
- in ocean surface temperature. *Paleoceanography*, Volume 27, pp. 1-17.
- 754 Bereiter, B. et al., 2015. Antarctic Ice Cores Revised 800KYr CO2 Data. Geophysical Research Letters, 42(2), pp.
- 755 542-549.
- 756 Betancourt, J. L., Van Devender, T. R. & Martin, P. S., 1990. Packrat middens: The last 40,000 years of biotic
- 757 *change*. Tucson: The University of Arizona Press.
- 758 Birkeland, P. W., Machette, M. N. & Haller, K. M., 1991. Soils as a tool for applied Quaternary geology. *Utah*
- 759 *Geological and Mineral Survey*, Volume Miscellaneous Publication 91-3, pp. 1-63.
- 760 Blaauw, M. & Christen, J. A., 2011. Flexible paleoclimate age-depth models using an autoregressive gamma
- process. Bayesian Analysis, Volume 6, pp. 457-474.
- Bonifacie, M. et al., 2017. Calibration of the dolomite clumped isotope thermometer from 25 to 350 C, and
- 763 implications for a universal calibration for all (Ca, Mg, Fe)CO3 carbonates. Geochimica et Cosmochimica Acta,
- 764 Volume 200, pp. 255-279.
- Bowling, D. R. et al., 2002. ¹³C content of ecosystem respiration is linked to precipitation and vapor pressure deficit.
- 766 *Oecologia*, Volume 131, pp. 113-124.
- Breecker, D. O., 2017. Atmospheric pCO₂ control on speleothem stable carbon isotope compositions. Earth and
- 768 Planetary Science Letters, Volume 458, pp. 58-68.
- Breecker, D. O. et al., 2012. Deep autotrophic soil respiration in shrubland and woodland ecosystems in central New
- 770 Mexico. *Ecosystems*, Volume 15, pp. 83-96.
- Preecker, D. O. et al., 2012. The sources and sinks of CO₂ in caves under mixed woodland and grassland vegetation.
- 772 Geochimica et Cosmochimica Acta, Volume 96, pp. 230-246.
- Breecker, D. O., Sharp, Z. D. & McFadden, L. D., 2009. Seasonal bias in the formation and stable isotopic
- composition of pedogenic carbonate in modern soils from central New Mexico, USA. *Geol Soc Amer Bull*, 121(3-4),
- 775 pp. 630-640.
- Cerling, T. E., 1984. The stable isotopic composition of modern soil carbonate and its relationship to climate. *Earth*
- 777 *Planet Scie Lett*, Volume 71, pp. 229-240.
- 778 Cerling, T. E. & Harris, J. M., 1999. Carbon isotope fractionation between diet and bioapatite in ungulate mammals
- and implications for ecological and paleoecological studies. *Oecologia*, Volume 120, pp. 347-363.
- 780 Coats, L. L., Cole, K. L. & Mead, J. I., 2008. 50,000 years of vegetation and climate history on the Colorado
- 781 Plateau, Utah and Arizona, USA. *Quaternary Research*, Volume 70, pp. 322-338.
- 782 Cole, D. R. & Monger, H. C., 1994. Influence of atmospheric CO₂ on the decline of C4 plants during the last
- deglaciation. *Nature*, Volume 368, pp. 533-536.
- Cole, K. L., Henderson, N. & Shafer, D. S., 1997. Holocene vegetation and historic grazing impacts at Capitol Reef
- National Park reconstructed using packrat middens. *Great Basin Naturalist*, 57(4), pp. 315-326.
- Coplen, T. B., 2007. Calibration of the calcite—water oxygen-isotope geothermometer at Devils Hole, Nevada, a
- natural laboratory. *Geochimica et Cosmochimica Acta*, 71(16), pp. 3948-3957.
- Davidson, G., 1995. The stable isotopic composition and measurement of carbon in soil CO₂. Geochimica et
- 789 *Cosmochimica Acta*, 59(12), pp. 2485-2489.
- Defliese, W. F., Hren, M. T. & Lohmann, K. C., 2015. Compositional and temperature effects of phosphoric acid
- fractionation on $\Delta 47$ analysis and implications for discrepant calibrations. *Chemical Geology*, Volume 396, pp. 51-
- 792 60
- 793 Dennis, K. J. et al., 2011. Defining an absolute reference frame for 'clumped' isotope studies of CO2. Geochimica et
- 794 *Cosmochimica Acta*, Volume 75, pp. 7117-7131.
- Diefendorf, A. F. et al., 2010. Global patterns in leaf ¹³C discrimination and implications for studies of past and
- 796 future climate. *PNAS*, 107(13), pp. 5738-5743.

- Dorale, J. A. & Liu, Z., 2009. Limitations of Hendy test criteria in judging the paleoclimatic suitability of
- 798 speleothems and the need for replication. *Journal of Karst and Cave Studies*, 71(1), pp. 73-80.
- Eggleston, S. et al., 2016. Evolution of the stable carbon isotope composition of atmospheric CO₂ over the last
- glacial cycle. *Paleoceanography*, Volume 31, pp. 434-452.
- Ehleringer, J. R., Cerling, T. E. & Helliker, B. R., 1997. C₄ photosynthesis, atmospheric CO₂, and climate.
- 802 *Oecologia,* Volume 112, pp. 285-299.
- 803 Ehleringer, J. R. & Monson, R. K., 1993. Evolutionary and ecological aspects of photosynthetic pathway variation.
- *Annual Review of Ecology and Systematics,* Volume 24, pp. 411-439.
- 805 Eiler, J., 2007. "Clumped-isotope" geochemistry The study of naturally-occurring, multiply-substituted
- isotopologues. Earth and Planetary Science Letters, Volume 262, pp. 309-327.
- Gazis, C. & Feng, X., 2004. A stable isotope study of soil water: evidence for mixing and preferential flow paths.
- 808 *Geoderma*, Volume 119, pp. 97-111.
- 809 Ghosh, P. et al., 2006. 13C–18O bonds in carbonate minerals: A new kind of paleothermometer. Geochimica et
- 810 *Cosmochimica Acta*, Volume 70, pp. 1439-1456.
- 811 Gile, L. H., Peterson, F. F. & Grossman, R. B., 1996. Morphological and genetic sequences of carbonate
- accumulation in desert soils. *Soil Science*, Volume 101, pp. 347-360.
- Hare, V. J., Loftus, E., Jeffrey, A. & Ramsey, C., 2018. Atmospheric CO₂ effect on stable carbon isotope
- composition of terrestrial fossil archives. *Nature Communications*, 9(252), pp. 1-8.
- Harris, R. N. & Chapman, D. S., 1997. Borehole temperatures and a baseline for 20th-century global warming
- 816 estimates. *Science*, Volume 275, pp. 1618-1621.
- Henkes, G. A. et al., 2013. Carbonate clumped isotope compositions of modern marine mollusk and brachiopod
- shells. *Geochimica et Cosmochimica Acta*, Volume 106, pp. 307-325.
- Higgins, R. W., Yao, Y. & Wang, X. L., 1997. Influence of the North American Monsoon system on the U.S.
- summer precipitation regime. *Journal of Climate*, Volume 10, pp. 2600-2622.
- 821 Holmgren, C. E., Norris, J. & Betancourt, J. L., 2007. Inferences about winter temperatures and summer
- precipitation from the Late Quaternary record of C₄ perennial grasses and C₃ desert shrubs in the northern
- 823 Chihuahuan Desert. *Journal of Quaternary Science*, 22(2), pp. 141-161.
- Horel, J. et al., 2020. Mesowest. [Online]
- 825 Available at: https://mesowest.utah.edu/
- 826 [Accessed 17 April 2020].
- Huth, T. E. et al., 2019. Seasonal bias in soil carbonate formation and its implications for interpreting high-
- resolution paleoarchives: evidence from southern Utah. JGR Biogeosciences, Volume 124, pp. 616-632.
- Hyland, E. G., Sheldon, N. D., Smith, S. Y. & Strömberg, C. A., 2019. Late Miocene rise and fall of C₄ grasses in
- the western United States linked to aridification and uplift. GSA Bulletin, Volume 131, pp. 224-234.
- Kemp, P. R., 1983. Phenological patterns of Chihuahuan Desert plants in relation to the timing of water availability.
- 832 *Journal of Ecology*, 71(2), pp. 427-436.
- Kim, S.-T. & O'Neil, J. R., 1997. Equilibrium and non-equilibrium oxygen isotope effects in synthetic carbonates.
- 634 *Geochimica et Cosmochimica Acta*, 61(16), pp. 3461-3475.
- Kita, N. T., Ushikubo, T., Fu, B. & Valley, J. W., 2009. High precision SIMS oxygen isotope analysis and the effect
- of sample topography. *Chemical Geology,* Volume 264, pp. 43-57.
- Kohn, M. J., 2010. Carbon isotope compositions of terrestrial C3 plants as indicators of (paleo)ecology and
- 838 (paleo)climate. *PNAS*, Volume 107, pp. 19691-19695.
- Kohn, M. J., 2016. Carbon isotope discrimination in C3 land plants is independent of natural variations in pco₂.
- 840 Geochem. Persp. Let., Volume 2, pp. 35-43.
- Kozdon, R. et al., 2009. Intratest oxygen isotope variability in the planktonic foraminifer N. pachyderma: Real vs.
- apparent vital effects by ion microprobe. *Chemical Geology*, 258(3-4), pp. 327-337.
- Lachniet, M. S., Denniston, R. F., Asmerom, Y. & Polyak, V. J., 2014. Orbital control of western North America
- atmospheric circulation and climate over two glacial cycles, *Nature Communications*, Volume 5, pp. 1-8.
- Liu, B., Phillips, F. M. & Campbell, A. R., 1996. Stable carbon and oxygen isotopes of pedogenic carbonates, Ajo
- 846 Mountains, southern Arizona: implications for paleoenvironmental change. *Palaeogeography, Palaeoclimatology*,
- 847 *Palaeoecology,* Volume 124, pp. 233-246.
- Madsen, D. B. et al., 2001. Late Quaternary environmental change in the Bonneville basin, western USA.
- 849 Palaeogeography, Palaeoclimatology, Palaeoecology, Volume 167, pp. 243-271.
- Marchetti, D. W. & Cerling, T. E., 2005. Cosmogenic 3He exposure ages of Pleistocene debris flows and desert
- pavements in Capitol Reef National Park, Utah. *Geomorphology*, Volume 67, pp. 423-435.

- Marchetti, D. W., Cerling, T. E. & Lips, E. W., 2005. A glacial chronology for the Fish Creek drainage of Boulder
- Mountain, USA, Utah. *Quaternary Research*, Volume 64, pp. 263-271.
- Marchetti, D. W. et al., 2011. Timing of glaciation and last glacial maximum paleoclimate estimates from the Fish
- Lake Plateau, Utah. *Quaternary Research*, Volume 75, pp. 183-195.
- McFadden, L. D., 2013. Strongly dust-influenced soils and what they tell us about landscape dynamics in vegetated
- 857 aridlands of the southwestern United States. In: M. Bickford, ed. The Web of Geological Sciences: Advances,
- 858 *Impacts, and Interactions*. s.l.:The Geological Society of America, pp. 501-532.
- Metcalfe, S. E., Barron, J. A. & Davies, S. J., 2015. The Holocene history of the North American Monsoon: 'known
- knowns' and 'known unknowns' in understanding its spatial and temporal complexity. Quaternary Science Reviews,
- 861 Volume 120, pp. 1-27.
- Monger, H. C., Cole, D. R., Gish, J. W. & Giordano, T. H., 1998. Stable carbon and oxygen isotopes in Quaternary
- soil carbonates as indicators of ecogeomorphic changes in the northern Chihuahuan Desert, USA. *Geoderma*,
- 864 Volume 82, pp. 137-172.
- Morris, J. L. et al., 2013. Holocene vegetation and fire reconstructions from the Aquarius Plateau, Utah, USA.
- 866 Quaternary International, Volume 310, pp. 111-123.
- Nordt, L., von Fischer, J. & Tieszen, L., 2007. Late Quaternary temperature record from buried soils of the North
- American Great Plains. *Geology*, 35(2), pp. 19-162.
- Oerter, E. J. & Amundson, R., 2016. Climate controls on spatial and temporal variations in the formation of
- pedogenic carbonate in the western Great Basin of North America. GSA Bulletin, 128(7-8), pp. 1-10.
- Oerter, E. J. et al., 2016. Pedothem carbonates reveal anomalous North American atmospheric circulation 70,000-
- 55,000 years ago. *PNAS*, Volume 113, pp. 919-924.
- Oster, J. L., Ibarra, D. E., Winnick, M. J. & Maher, K., 2015. Steering of westerly storms over western North
- America at the Last Glacial Maximum. *Nature Geoscience*, Volume 8, pp. 201-205.
- Passey, B. H. & Cerling, T. E., 2006. In situ stable isotope analysis (δ^{13} C, δ^{18} O) of very small teeth using laser
- ablation GC/IRMS. *Chemical Geology*, Volume 235, pp. 238-249.
- Passey, B. H. et al., 2014. Triple oxygen isotopes in biogenic and sedimentary carbonates. *Geochimica et*
- 878 *Cosmochimica Acta*, Volume 141, pp. 1-25.
- 879 Prism Climate Group, 2018. PRISM Climate Data. [Online]
- 880 Available at: http://prism.oregonstate.edu
- 881 [Accessed 26 January 2018].
- Pustovoytov, K., Schmidt, K. & Parzinger, H., 2007. Radiocarbon dating of thin pedogenic carbonate laminae from
- Holocene archeological sites. *The Holocene*, 17(6), pp. 835-843.
- Pustovoytov, K., Schmidt, K. & Taubald, H., 2007. Evidence for Holocene environmental changes in the Fertile
- 885 Crescent provided by pedogenic carbonate coatings. *Quaternary Research*, Volume 67, pp. 315-327.
- Quade, J., 2014. The carbon, oxygen, and clumped isotopic composition of soil carbonate in archeology. *Treatise of*
- 887 *Geochemistry,* Volume 14, pp. 129-143.
- 888 Quade, J., Cerling, T. E. & Bowman, J. R., 1989. Systematic variations in the carbon and oxygen isotopic
- 889 composition of pedogenic carbonate along elevation transects in the southern Great Basin, United States. Geological
- 890 Society of America Bulletin, Volume 101, pp. 464-475.
- Reimer, P. J. et al., 2013. IntCall3 and Marine 13 radiocarbon age calibration curves 0-50,000 yr cal BP.
- 892 *Radiocarbon*, 55(4), pp. 1869-1887.
- 893 Romanek, C. S., Grossman, E. L. & Morse, J. W., 1992. Carbon isotopic fractionation in synthetic aragonite and
- calcite: Effects of temperature and precipitation rate. *Geochimica et Cosmochimica Acta*, Volume 56, pp. 419-430.
- Schauer, A. J., Kelson, J., Saenger, C. & Huntington, K. W., 2016. Choice of ¹⁷O correction affects clumped isotope
- 896 (Δ_{47}) values of CO₂ measured with mass spectrometry. Rapid Communications in Mass Spectrometry, Volume 30,
- 897 pp. 2607-2616.
- Schmidt, G. A., Bigg, G. R. & Rohling, E. J., 1999. Global Seawater Oxygen-18 Database v1.22. [Online]
- Available at: https://data.giss.nasa.gov/o18data/
- 900 [Accessed 25 May 2018].
- 901 Schmitt, D. N. & Lupo, K. D., 2012. The Bonneville Estates Rockshelter rodent fauna and changes in Late
- Pleistocene-Middle Holocene climates and biogeography in the Northern Bonneville Basin, USA. *Quaternary*
- 903 *Research*, Volume 78, pp. 95-102.
- Schubert, B. A. & Jahren, A. H., 2012. The effect of atmospheric CO₂ concentration on carbon isotope fractionation
- 905 in C₃ land plants. *Geochimica et Cosmochimica Acta*, Volume 96, pp. 29-43.
- Schubert, B. A. & Jahren, A. H., 2018. Incorporating the effects of photorespiration into terrestrial paleoclimate
- 907 reconstruction. *Earth-Science Reviews*, Volume 177, pp. 637-642.

- 908 Schuman, B. N. & Serravezza, M., 2017. Patterns of hydroclimatic change in the Rocky Mountains and surrounding
- 909 regions since the last glacial maximum. *Quaternary Science Reviews*, Volume 173, pp. 58-77.
- Shurtliff, R. A. et al., 2017. A 13 000 year multi-proxy climate record from central Utah (western USA),
- emphasizing conditions leading to mass movements. *Boreas*, Volume 46, pp. 308-324.
- 912 Sprenger, M., Leistert, H., Gimbel, K. & Weiler, M., 2016. Illuminating hydrological processes at the soil-
- vegetation-atmosphere interface with water stable isotopes. *Reviews of Geophysics*, Volume 54, pp. 674-704.
- 914 Steponaitis, E. et al., 2015. Mid-Holocene drying of the U.S. Great Basin recorded in Nevada speleothems.
- 915 Quaternary Science Reviews, Volume 127, pp. 174-185.
- Sun, Y., Clemens, S. C., An, Z. & Yu, Z., 2006. Astronomical timescale and paleoclimatic implication of stacked
- 3.6-Myr monsoon records from the Chinese Loess Plateau. *Quaternary Science Reviews*, Volume 25, pp. 33-48.
- Teeri, J. A. & Stowe, L. G., 1976. Climatic patterns and the distribution of C₄ grasses in North America. *Oecologia*,
- 919 Volume 23, pp. 1-12.
- 920 Teeri, J. A., Stowe, L. G. & Livingstone, D. A., 1980. The distribution of C₄ species of the Cyperaceae in North
- America in relation to climate. *Oecologia*, Volume 47, pp. 307-310.
- 922 Tipple, B. J. & Pagani, M., 2007. The early origins of terrestrial C₄ photosynthesis. Annu. Rev. Earth Planet. Sci.,
- 923 Volume 35, pp. 435-461.
- 924 Treadwell-Steitz, C. & McFadden, L. D., 2000. Influence of parent material and grain size on carbonate coatings in
- gravelly soils, Palo Duro Wash, New Mexico. *Geoderma*, Volume 94, pp. 1-22.
- Tukey, J. W., 1977. Exploratory Data Analysis. Reading, MA: Addison-Wesley Publishing Co..
- Turnier, R. B. et al., 2019. Calibration of oxygen isotope fractionation and calcite-corundum thermometry in emery
- at Naxos, Greece. *Journal of Metamorphic Geology*, Volume 00, pp. 1-18.
- Valley, J. W. & Kita, N. T., 2009. In situ oxygen isotope geochemistry by ion microprobe. In: F. M., ed. MAC Short
- Course: Secondary Ion Mass Spectrometry in the Earth Sciences. s.l.:vol. 41, pp. 19-63.
- Wentworth, T. R., 1983. Distribution of C₄ plants along environmental and compositional gradients in southeastern
- 932 Arizona. Vegetatio, Volume 52, pp. 21-34.
- Williford, K. H. et al., 2013. Preservation and detection of microstructural and taxonomic correlations in the carbon
- isotopic compositions of individual Precambrian microfossils. *Geochimica et Cosmochimica Acta*, Volume 104, pp.
- 935 165-182.
- 936 WiscSIMS, 2018. The Wisconsin Secondary Ion Mass Spectrometer Laboratory. [Online]
- 937 Available at: http://www.geology.wisc.edu/facilities/wiscsims/
- 938 [Accessed 6 March 2018].
- Wycech, J. B. et al., 2018. Comparison of δ^{18} O analyses on individual planktonic foraminifer (Orbulina universa)
- shells by SIMS and gas-source mass spectrometry. *Chemical Geology,* Volume 483, pp. 119-130.

Figures

Figure 1: Overview of the Capitol Reef region showing rind collection site (yellow star), local paleoclimate record locations (red dots), and nearby geographic points. Inset to top right shows a topographic map of Utah with a dashed line approximating the limit of the Colorado Plateau and a star denoting Torrey. See SI Appendix, Fig. S1 for a close-up of the Torrey region. Inset to bottom right shows Torrey region interpolated PRISM 30 year climate normal with precipitation (blue bar graph) and temperature (red line). Image is from Google Earth Pro.



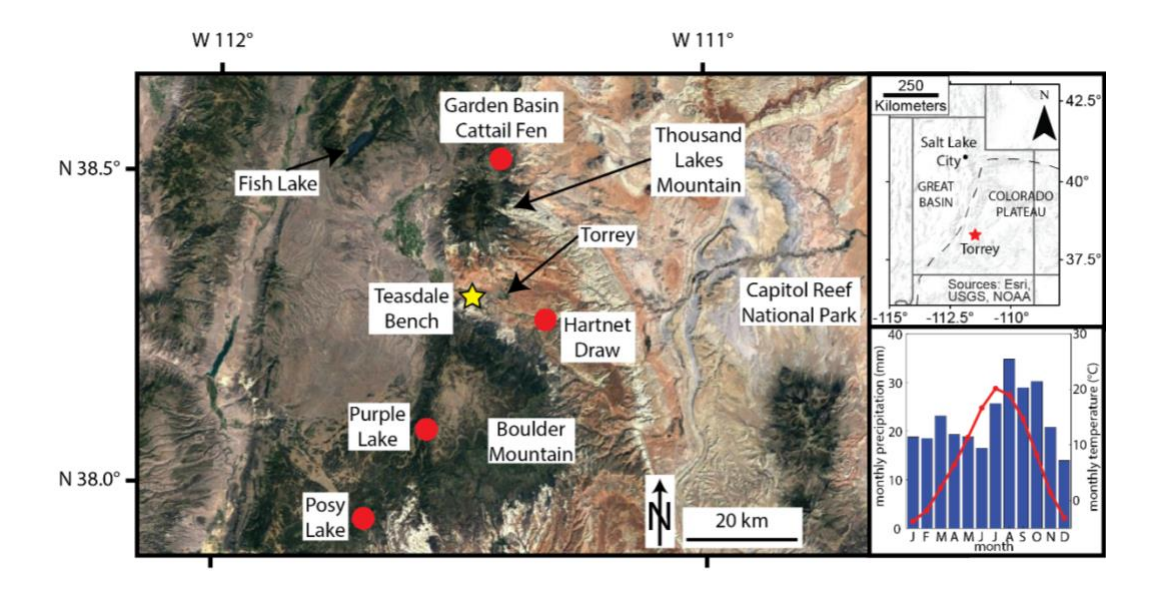


Figure 2: Carbonate rind overview. (a) Boulder overturned during road construction near Teasdale Junction, Utah. Boulder surface color indicates soil horizons from when the boulder was in the ground; 1 – exposed boulder surface, 2 – Ca²⁺ leaching zone, and 3 – calcite accumulation zone (Huth, et al., 2019). (b) Cross section of Pendant 11-8 that formed on the bottom of a boulder. (c) SEM secondary electron image showing rind structure and analysis spots.

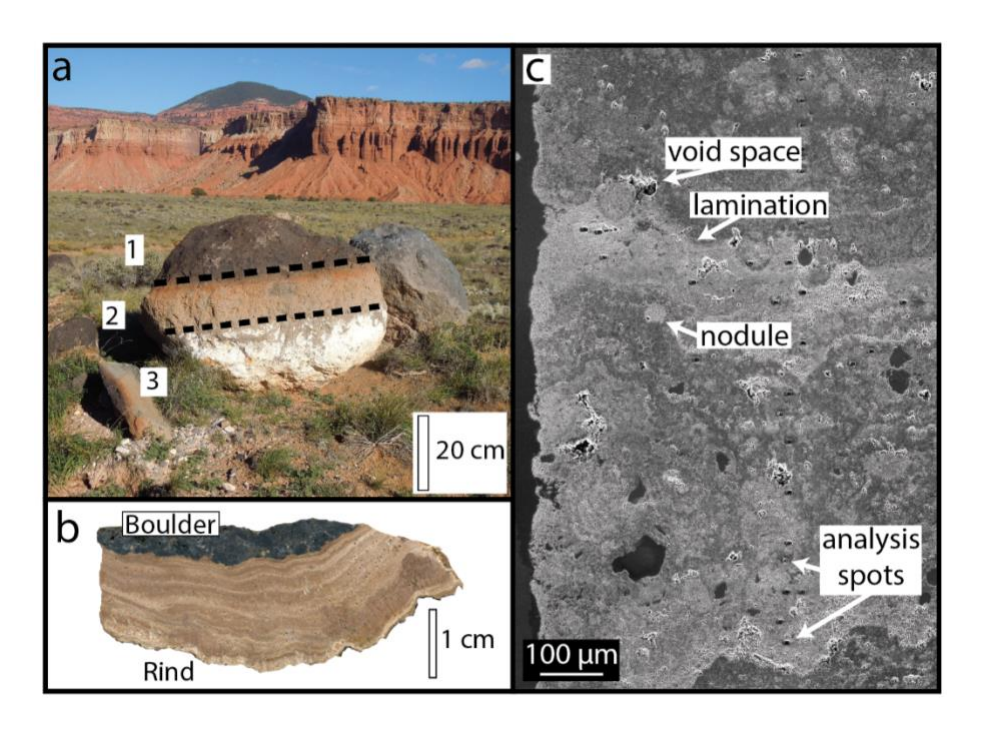


Figure 3: Modern soil data from the study region compiled as day of year (DOY). All data were collected between 35 and 45 cm depth unless otherwise noted. (a) Soil CO₂ (black dots) and $\delta^{13}C_{\text{soil-respiration}}$ (red triangles). Red line is a sinusoidal fit to the $\delta^{13}C_{\text{soil-respiration}}$ data. The sharp decreases in soil CO₂ near days 205 and 270 (July and September) may be an instrumental artifact due to intense rainfall. (b) Soil temperature (black dots), $\delta^{18}O_{\text{precipitation}}$ (red triangles), and $\delta^{18}O_{\text{soil-water}}$ (blue squares). Blue line is a sinusoidal fit to the $\delta^{18}O_{\text{soil-water}}$ data. The red bar represents the average Holocene temperature of soil carbonate formation derived from Δ₄₇ analyses (Huth, et al., 2019). The $\delta^{18}O_{\text{soil-water}}$ data represent samples from 35–100 cm depth. (c) Soil moisture. Note soil isotope data were collected during different years from the environmental data and thus should only be interpreted in terms of general seasonal trends (2015–2017 and 2014–2015, respectively). See (Huth, et al., 2019) for details and original dataset.

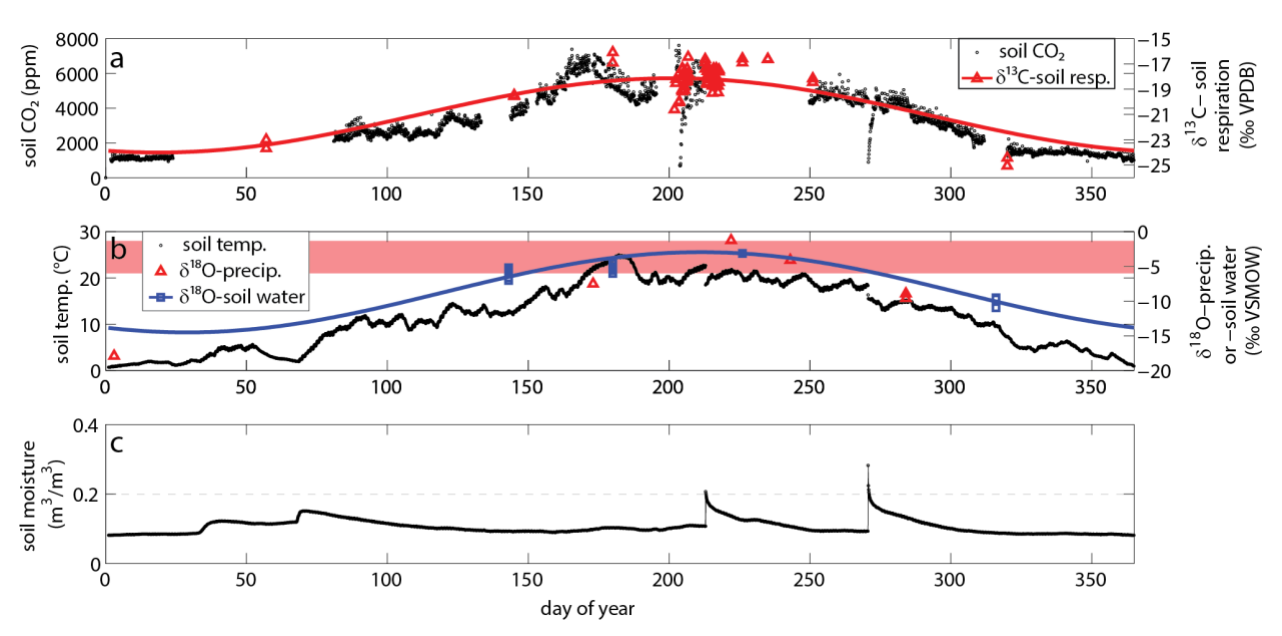


Figure 4: Age model considerations. (a and b) Age model construction. Marker layers in the (a) milled piece of Pendant 11-8 and (b) the SIMS mount for Transect 1. Marker layers are outlined in (a) and shown on the left edge in (b). The thick black line in (b) follows the transect of SIMS analysis spots used in this study (individual spots are not visible at this scale, see also Fig. 2). The transect varies from a straight line where we avoided nodules or had to analyze several locations to acquire a suitable analysis. (c) The radiocarbon age model for Pendant 11-8 from the Bacon age-modelling program (Blaauw & Christen, 2011). The model uses "% through rind" to normalize for variable thickness along individual transects (see *section 2. Study setting and methodology*). Upper panels depict the distribution of Markov Chain Monte Carlo (MCMC) iterations (left panel), and the prior (green curves) and posterior (grey histograms) distributions for the accumulation rate (middle panel) and memory (right panel). Bottom panel shows the age model. Yellow shapes with thick black outlines are contours of calibrated radiocarbon dates (size is exaggerated for visibility). Darker shading indicates more likely calendar ages along the age model, gray curves are the 95% confidence intervals, and red curve is the "best" model based on the mean age for each depth. See also SI Appendix Tables S3–S5 and Figures S2–S4 for additional information.

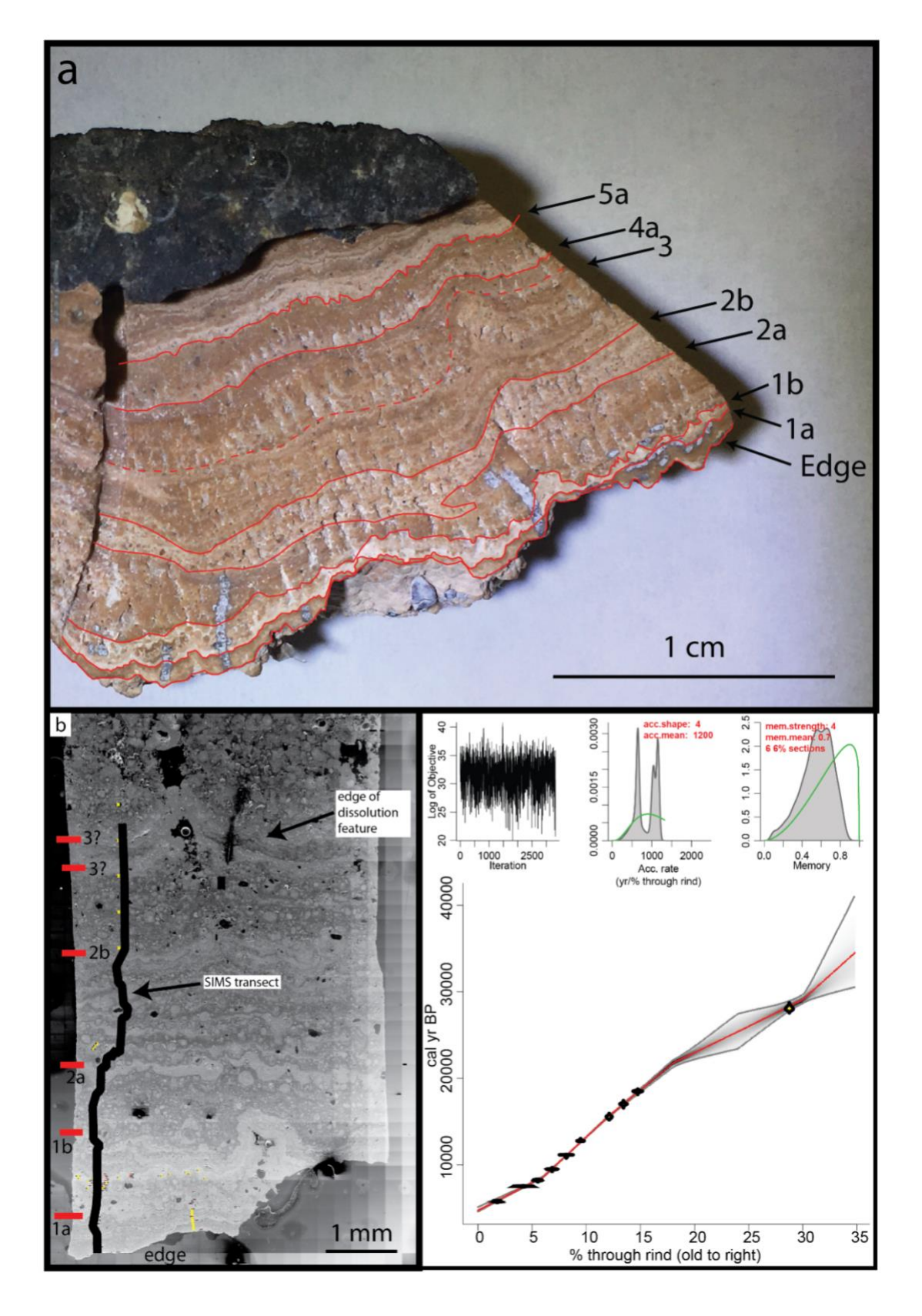


Figure 5: Laminated soil carbonate isotope records. (a) Soil carbonate δ^{13} C and (b) δ^{18} O records from SIMS, this study. Red and blue symbols are two transects from Pendant 11-8 (average ± 2 SD precision of ± 0.2 % for δ^{18} O and ± 0.8 % for δ^{13} C are short vertical lines in the upper left corners) and thick lines are 1,000-yr window moving averages (1,000-yr MA). Radiocarbon dates are black squares at the bottom. (c) Formation temperature estimates (Defliese, et al., 2015) through time for this study showing individual measurements (red circles), sample averages (black x's, note not all samples have replicates), and sample 95% confidence intervals. Horizontal bars show 1 standard error (dark red) and the 95% confidence interval (light pink) for data within an interval (see text for details). Modern JJAS average, minimum, and maximum soil temperature are shown by the yellow star with black lines, respectively (data for years 2014-2015 from (Huth, et al., 2019)).

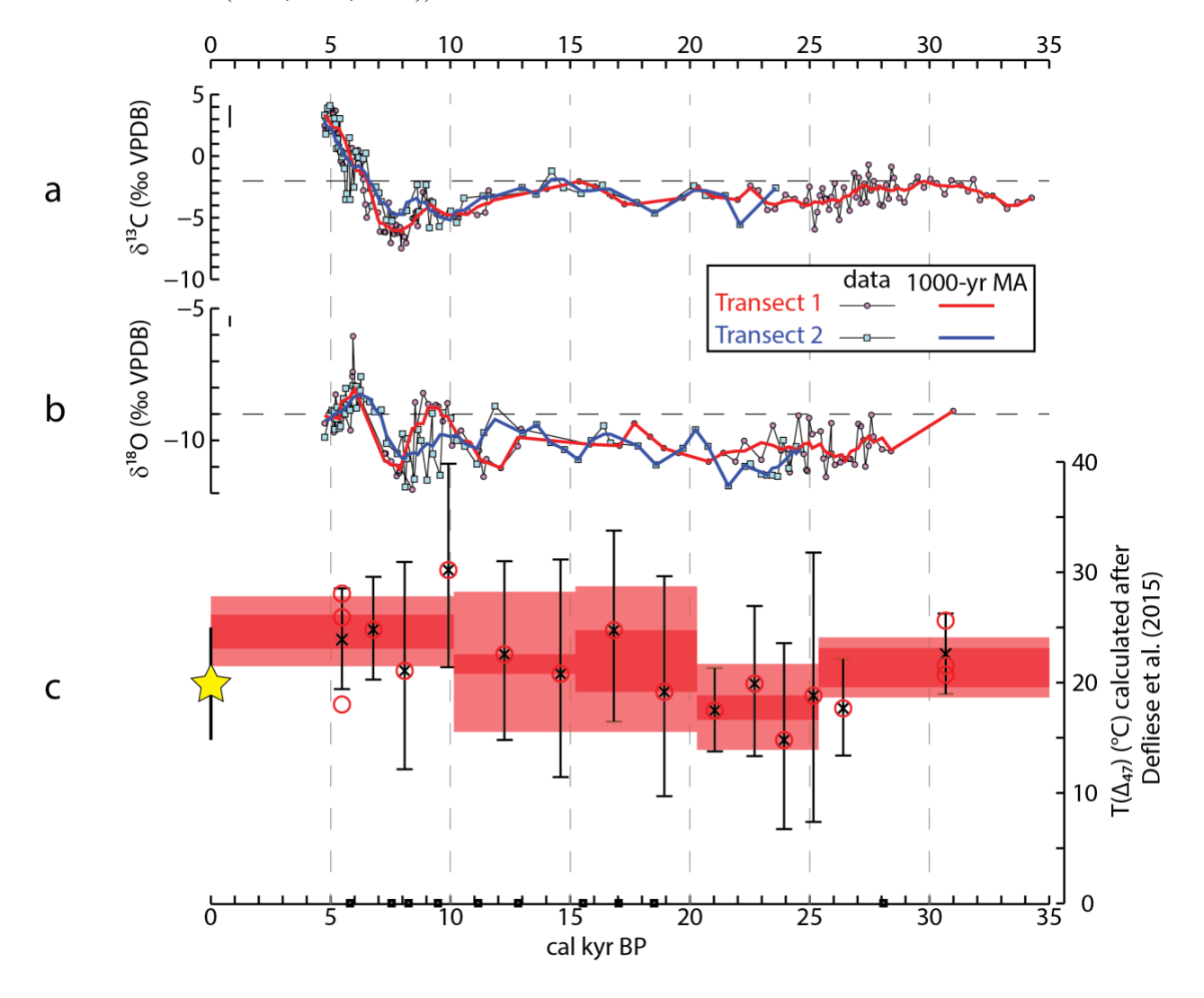


Figure 6: Paleovegetation reconstruction at Torrey, UT. Only Transect 1 is shown for clarity (see Transect 2 in SI Appendix, Fig. S7). (a) $\delta^{13}C_{sc}$ as in Fig. 5. (b) Modeled $\delta^{13}C_{soil-respiration}$ with gray bar representing modern observed range during June-August. (c) Modeled %C₃ plants for two different C₃ endmembers (red triangles = -21.4 % VPDB; black circles = -30 % VPDB). Both scenarios use a C₄ endmember of -10 % VPDB and are constrained by soil $CO_2 \ge 1,000$ ppm. The overlapping red and gray bands correspond to the two endmember scenarios and show the modern observed range during June-August transposed into %C₃ plants. Note the inverted y-axis in (c).

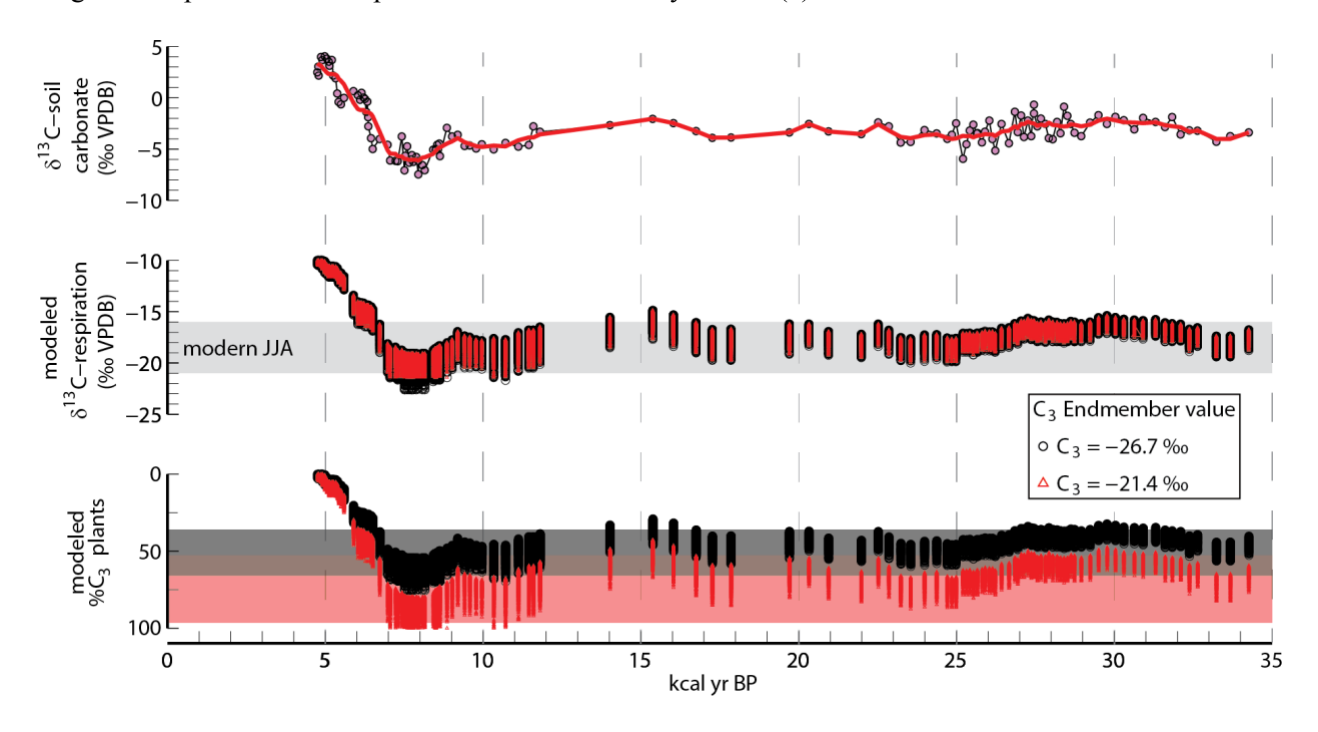


Figure 7: Reconstructed $\delta^{18}O_{soil-water}$ and regional proxy comparison. (a) Modeled $\delta^{18}O_{soil-water}$ (this study). Transect colors and temperature intervals are as in Fig. 5, with the darker fill calculated from the temperature estimate standard error and the lighter fill calculated from the 95% confidence interval. Gray bars show the range of values for modern soil water in November and June-August, respectively (Fig. 3). (b) Record of $\delta^{18}O_{calcite}$ for a speleothem from Pink Panther Cave, New Mexico (Asmerom, et al., 2007). Black line is a 1,000-yr window moving average. (c) Compilation of when USA Rocky Mountain lakes were anomalously low (Schuman & Serravezza, 2017). (d) Terminal and recessional moraines from the Last Glacial Maximum and the late Pinedale on Boulder Mountain (BM) and Fish Lake (FL), which is on Fish Lake Mountain (Marchetti, et al., 2005; Marchetti, et al., 2011) (Fig. 1). Note the inverted y-axes in (b) and (c).

